AGU PUBLICATIONS

JGR

Journal of Geophysical Research: Atmospheres

RESEARCH ARTICLE
10.1002/2015JD024595

Key Points:
- Using distributions of updraft velocity and lapse rate increases droplet spectral width
- Organic hygroscopicity changes cloud drop only for high concentrations near critical diameter
- Changes in drop spectral width cause larger reflectivity differences than organic hygroscopicity

Supporting Information:
- Supporting Information S1

Correspondence to:
L. M. Russell,
lmrussell@ucsd.edu

Citation:
Sanchez, K. J., et al. (2016), Meteorological and aerosol effects on marine cloud microphysical properties, *J. Geophys. Res. Atmos.*, *121*, 4142–4161, doi:10.1002/2015JD024595.

Received 13 DEC 2015
Accepted 21 MAR 2016
Accepted article online 29 MAR 2016
Published online 25 APR 2016

Meteorological and aerosol effects on marine cloud microphysical properties

K. J. Sanchez[1], L. M. Russell[1], R. L. Modini[1,2], A. A. Frossard[1,3], L. Ahlm[1], C. E. Corrigan[1], G. C. Roberts[1,4], L. N. Hawkins[5], J. C. Schroder[6,7], A. K. Bertram[6], R. Zhao[8], A. K. Y. Lee[8], J. J. Lin[9], A. Nenes[10], Z. Wang[11], A. Wonaschütz[12], A. Sorooshian[11], K. J. Noone[13], H. Jonsson[14], D. Toom[15], A. M. Macdonald[15], W. R. Leaitch[15], and J. H. Seinfeld[16]

[1]Scripps Institution of Oceanography, University of California, San Diego, La Jolla, California, USA, [2]Now at École Polytechnique Fédérale de Lausanne, Lausanne, Switzerland, [3]Now at Department of Chemistry, University of California, Berkeley, California, USA, [4]Centre National de la Recherche Scientifique–Groupe d'études de l'Atmosphère Météorologique, Toulouse, France, [5]Department of Chemistry, Harvey Mudd College, Claremont, California, USA, [6]Department of Chemistry, University of British Columbia, Vancouver, British Columbia, Canada, [7]Now at Department of Chemistry and Biochemistry and CIRES, University of Colorado Boulder, Boulder, Colorado, USA, [8]Department of Chemistry, University of Toronto, Toronto, Ontario, Canada, [9]School of Earth and Atmospheric Sciences, Georgia Institute of Technology, Atlanta, Georgia, USA, [10]School of Earth and Atmospheric Sciences and School of Chemical and Biomolecular Engineering, Georgia Institute of Technology, Atlanta, Georgia, USA, [11]Department of Chemical and Environmental Engineering and Department of Atmospheric Sciences, University of Arizona, Tucson, Arizona, USA, [12]Faculty of Physics, University of Vienna, Vienna, Austria, [13]Department of Environmental Science and Analytical Chemistry, Stockholm University, Stockholm, Sweden, [14]Center for Interdisciplinary Remotely-Piloted Aerosol Studies, Marina, California, USA, [15]Science and Technology Branch, Environment Canada, Toronto, Ontario, Canada, [16]Department of Chemical Engineering, California Institute of Technology, Pasadena, California, USA

Abstract Meteorology and microphysics affect cloud formation, cloud droplet distributions, and shortwave reflectance. The Eastern Pacific Emitted Aerosol Cloud Experiment and the Stratocumulus Observations of Los-Angeles Emissions Derived Aerosol-Droplets studies provided measurements in six case studies of cloud thermodynamic properties, initial particle number distribution and composition, and cloud drop distribution. In this study, we use simulations from a chemical and microphysical aerosol-cloud parcel (ACP) model with explicit kinetic drop activation to reproduce observed cloud droplet distributions of the case studies. Four cases had subadiabatic lapse rates, resulting in fewer activated droplets, lower liquid water content, and higher cloud base height than an adiabatic lapse rate. A weighted ensemble of simulations that reflect measured variation in updraft velocity and cloud base height was used to reproduce observed droplet distributions. Simulations show that organic hygroscopicity in internally mixed cases causes small effects on cloud reflectivity (CR) (<0.01), except for cargo ship and smoke plumes, which increased CR by 0.02 and 0.07, respectively, owing to their high organic mass fraction. Organic hygroscopicity had larger effects on droplet concentrations for cases with higher aerosol concentrations near the critical diameter (namely, polluted cases with a modal peak near 0.1 μm). Differences in simulated droplet spectral widths (k) caused larger differences in CR than organic hygroscopicity in cases with organic mass fractions of 60% or less for the cases shown. Finally, simulations from a numerical parameterization of cloud droplet activation suitable for general circulation models compared well with the ACP model, except under high organic mass fraction.

1. Introduction

Clouds play an essential role in the climate system. Cloud reflectivity (CR) is determined by microphysical properties, such as cloud droplet number concentration (CDNC), size distribution, cloud thickness, and liquid water content (LWC). Atmospheric chemical transport models and aerosol-cloud modules embedded in general circulation models (GCMs) predict CDNC and a single volumetric or effective droplet size resulting from the activation of aerosols. Though knowledge of the cloud droplet size distribution is important for accurately estimating CR, many atmospheric models do not include this level of detail. Clouds form when aerosols undergo activation in conditions of water vapor supersaturation. The aerosol characteristics that are important in-cloud droplet activation are size, concentration, and chemical composition. A key property of aerosol-cloud interactions related to aerosol chemical composition is hygroscopicity.

The basis of microscale models for simulating the formation of liquid phase clouds is a solution of the conservation equations for energy and water vapor. As an air parcel cools to below the dew point, water vapor becomes supersaturated, and droplets start forming on those particles that can act as cloud condensation nuclei (CCN). Not all aerosol particles are CCN. Particles with greater mass have more soluble mass and reduced curvature effects, enhancing their ability to become CCN; hydrophilic particles are more water soluble, increasing their effectiveness as CCN. Each particle therefore requires exposure to a characteristic level of supersaturation to act as a CCN. The supersaturation, s, that develops in clouds is set by a dynamic balance between adiabatic cooling (that increases s) and condensation upon existing droplets (that decreases s). During the initial phases of cloud formation, cooling dominates, and s increases and drives the formation of droplets. A point is reached, however, where water vapor condensation becomes dominant, s is reduced, and droplet nucleation ceases. The point of maximum supersaturation, s_{max}, is therefore the quantity that determines how many particles can act as a CCN. Because of this, CDNC and size are dependent on updraft velocity, aerosol size distribution, and chemical composition. Globally, regimes have been identified in which cloud formation is controlled mainly by updraft velocity and others in which formation is governed by CCN properties [*Reutter et al.*, 2009]. For example, at high aerosol number concentrations characteristic of polluted conditions and low updraft conditions, CDNC is more sensitive to changes in updraft velocity or supersaturation [*McFiggans et al.*, 2006]. Previous work has shown that CDNC is better represented in models with a more realistic distribution of updraft velocities, rather than a single updraft value [*Conant et al.*, 2004; *Peng et al.*, 2005; *Snider et al.*, 2003]. *Hudson and Noble* [2014] found strong evidence from measurements showing variations in CDNC that were due to the steep slope of the CCN concentration with supersaturation, providing observational evidence for a case in which CDNC is sensitive to updraft velocity. Global climate models have also been used to show that a characteristic velocity cannot reproduce the indirect aerosol effects of a distribution of updraft velocities and that the uncertainty in the width of the vertical velocity distribution can perturb the radiative flux by up to 0.4 W m^{-2} [*West et al.*, 2014]. Variations in updraft velocity can contribute to the broadening of the cloud droplet distribution [*Hsieh et al.*, 2009], as each updraft leads to a different droplet size distribution. The droplet size distribution needs to be modeled accurately to estimate cloud optical properties. The droplet size is also a function of LWC, so the resolution of LWC is important for accurate modeling of cloud systems. Finally, since cloud thickness is also important for cloud optical properties, cloud base height needs to be simulated accurately. Cloud base height is a function of several variables, one of which is lapse rate [*Li et al.*, 2013]. The value of the lapse rate varied to show the sensitivity of cloud droplet distribution to both lapse rate and cloud base height.

Activation of inorganic salt particles is a well-understood parameterized process in models. In general, however, organic compounds constitute a substantial fraction of atmospheric aerosols. Studies focusing on analysis of organic aerosol properties have shown that organic components exhibit a wide range of water solubility. Unlike that of most inorganic aerosol components, the hygroscopicities of organic compounds are less constrained. Laboratory studies have demonstrated that purely organic particles can act as CCN [*Cruz and Pandis*, 1997; *Novakov and Corrigan*, 1996; *Raymond and Pandis*, 2002]. Studies have also shown that organic hygroscopicity can increase when internally mixed with even a small fraction of inorganic components if the inorganic water content modifies slightly soluble organic compounds into dissolved compounds [*Collins et al.*, 2013; *Shulman et al.*, 1996]. *Cruz and Pandis* [2000] showed evidence of several organic-salt mixtures in which there was no change in the individual water absorption of each component, indicating that simple volume mixing rules could be applied. *Wang et al.* [2010] showed that CCN concentrations were within 20% when an internal mixture was assumed. However, these lab experiments investigating internal mixture thermodynamic interactions have used mixtures containing only a few known compounds. The thermodynamics of more complex organic-containing mixtures is not well understood, although several approaches have been used with success [*Ming and Russell*, 2004; *Petters et al.*, 2015]. In addition, the available measurements of organic ambient aerosol composition are typically not quantified by individual molecules. Given this support for volume mixing and the lack of organic molecular composition that would be needed to support another approach, the aerosol-cloud parcel (ACP) model simulations have relied on the assumption of volume mixing.

Modeling the cloud droplet activation of mixed inorganic-organic aerosols representative of real-world air masses remains a frontier area of cloud physics. This is in part owing to compositional heterogeneity of particle types, leading to an externally mixed aerosol population. Near urban regions, tandem differential mobility analyzer [*Massling et al.*, 2009; *Tiitta et al.*, 2010], single-particle mass spectrometry [*Healy et al.*, 2014], and optical microscopy [*Moffet et al.*, 2010] show evidence of multiple-particle populations, especially in regard to their carbonaceous content. In continental outflow [*Hawkins et al.*, 2010; *Hegg et al.*, 2010; *Leaitch et al.*, 2010], free tropospheric air masses and fresh biogenic aerosol production [*Allan et al.*, 2009; *Hersey et al.*, 2009; *Mochida et al.*, 2011], less hygroscopic and hydrophobic modes of particles are observed. To accurately represent the effects of aerosol chemical composition on activation of cloud droplets, it is important to know the contribution of organic mass to each population. In understanding cloud formation and properties in different regions of the atmosphere, it is important to compare the results of detailed simulations with actual measured aerosol and cloud properties.

In this work, the comparison of models of marine cloud formation with actual field measurements of organic aerosols and cloud droplets is of particular interest. We focus on observations from two field studies, the Eastern Pacific Emitted Aerosol Cloud Experiment (E-PEACE) and Stratocumulus Observations of Los-Angeles Emissions Derived Aerosol-Droplets (SOLEDAD). Each of these experiments was carried out in the eastern Pacific off the coast of California, in a region characterized by ship exhaust and smoke from land-based fires, as well as natural marine aerosol sources, such as bubble bursting at the ocean surface [*Facchini et al.*, 2008; *Frossard*, 2014; *Leck and Bigg*, 2005; *Quinn et al.*, 2014] and oxidation of dimethyl sulfide (by hydroxyl radicals) to produce sulfuric acid.

We use a detailed chemical and microphysical aerosol-cloud parcel (ACP) model with explicit kinetic droplet activation to simulate observed cloud droplet distribution and composition. Novel aspects of this modeling study include the extensive nature of the measured constraints (on not only cloud thermodynamic properties but also initial particle number distribution and composition) as well as resulting cloud drop distribution and composition that are available from these two eastern Pacific stratocumulus experiments. These detailed case studies allow evaluation of the extent to which the model effectively represents processes of cloud droplet formation. To identify the effect of lapse rate and updraft variation on droplet spectral widths (k), distributions of each are used as model inputs. Also, to identify the contribution of organic components to droplet formation, we simulate the effect of smoke-generated plumes, a cargo ship plume, and background aerosol. We then evaluate the sensitivity of the predictions to the organic aerosol fraction and to the hygroscopicity of the aerosol. In addition, ACP model simulations are compared to those from a numerical GCM parameterization of cloud droplet activation [*Betancourt and Nenes*, 2014; *Fountoukis and Nenes*, 2005; *Nenes and Seinfeld*, 2003] to evaluate the accuracy of the more efficient approach in the GCM. Finally, to put the meteorological and microphysical effects in context of radiative forcing, we investigate the sensitivity of cloud reflectance (at measurement heights) to simulated droplet spectra for six cases.

2. Methods

This section summarizes measurements from two field campaigns, E-PEACE off the coast of California in July and August 2011 and SOLEDAD in May and June 2012 located 1 km from the coast, and the models used to simulate the observations.

2.1. E-PEACE

E-PEACE consisted of a 12 day research cruise on the R/V *Point Sur* (12 to 23 July) and 30 research flights on the Center for Interdisciplinary Remotely-Piloted Aircraft Studies (CIRPAS) Twin Otter aircraft (8 July to 18 August). Both the ship and aircraft were equipped with an array of instruments to provide detailed meteorological and aerosol measurements [*Russell et al.*, 2013]. The two E-PEACE case studies considered here occurred on 16 July (EJL16) and 10 August (EAG10). Each case includes a background “B” case (EJL16B and EAG10B) and a plume “P” case (EJL16P and EAG10P). The EJL16P case included release of organic smoke from two U.S. Army-issued smoke generators to produce concentrated plumes of particles consisting of vaporized and condensed paraffin oil [*Russell et al.*, 2013; *Wonaschuetz et al.*, 2013]. In the EAG10P case the Twin Otter aircraft sampled exhaust from a cargo ship.

2.1.1. R/V *Point Sur* Ship Measurements

A vertical inlet, shielded from sea spray, on the forward deck of the R/V *Point Sur* was used to sample air. Aerosols were dried in diffusion driers before delivery to instruments. A Scanning Electrical Mobility Sizer (SEMS, Model 138, 2002, BMI, Hayward, CA) was used to measure the number size distribution of submicrometer (0.01–0.9 μm diameter) particles. Supermicrometer particle size distributions were measured using an Aerodynamic Particle Sizer (APS 3321, TSI Inc., St. Paul, MN, size range 0.5–20 μm). The total number

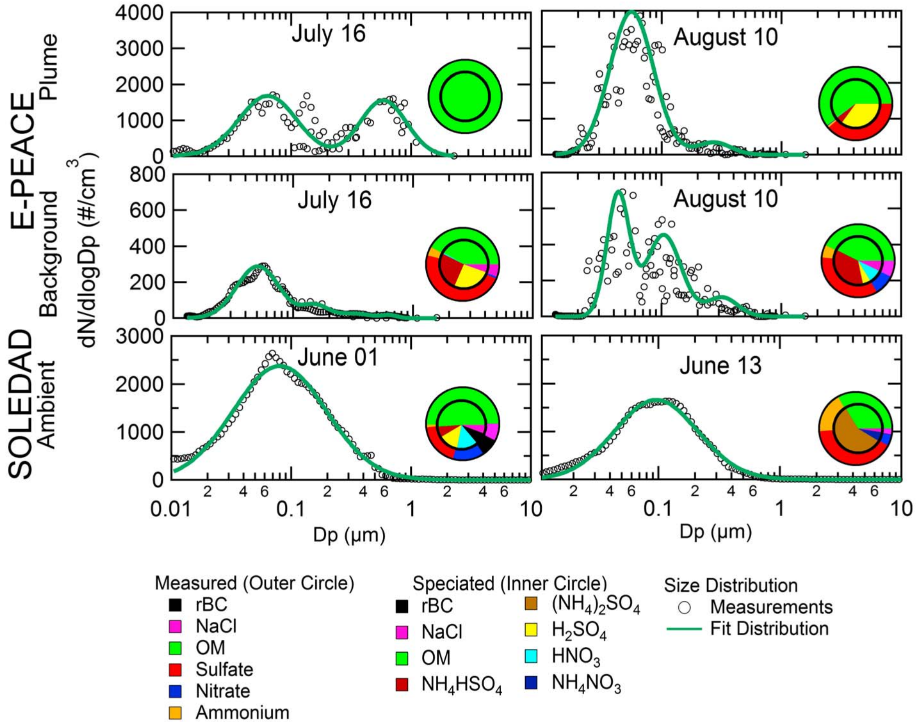

Figure 1. Below-cloud dried particle number distributions with lognormal fits for each case study. The pie charts show measured submicron and molecular composition from an SP2, refractory black carbon (rBC), and an AMS with scaled NaCl [*Modini et al*., 2015] and organic mass (OM). The 16 July submicrometer measurements of aerosol size and composition were collected on the R/V *Point Sur* (1717–1722 LT) with a SEMS and HR-ToF-AMS, respectively; 10 August submicrometer measurements of aerosol size and composition were collected on the CIRPAS Twin Otter (1710–1716 LT) with a scanning DMA and C-ToF-AMS, respectively. The SOLEDAD submicrometer measurements of aerosol size and composition from 1 (1200–1650 LT) and 13 (0800–1050 LT) June were collected on Mount Soledad with a SEMS and HR-ToF-AMS, respectively. E-PEACE measurements also include PCASP measurements for supermicron aerosol sizes (0.1–10 μm). The size distribution and composition in this figure are used as input for the cases shown in Table 1.

concentration of aerosol particles was tracked with a condensation particle counter (CPC 3010, TSI Inc., St. Paul, MN) to monitor contamination from the R/V *Point Sur* stack and from nearby ships. Submicrometer particles were separated from supermicrometer particles with a cyclone (sharp cut cyclone SCC 2.229, BGI Inc., U.S.) then analyzed with a high-resolution time-of-flight aerosol mass spectrometer (HR-ToF-AMS, Aerodyne Research Inc., Billerica, MA) to measure nonrefractory inorganic (sulfate, ammonium, nitrate, and chloride) and organic components [*DeCarlo et al*., 2006]. For the HR-ToF-AMS, a collection efficiency of 0.6 and a detection limit of 0.01 $\mu g\,m^{-3}$ were applied [*Wonaschuetz et al*., 2013]. Refractory black carbon was measured with a single-particle soot photometer (SP2, DMT, Boulder, CO), which has a particle size range of 80–300 nm; refractory black carbon concentrations were negligible during E-PEACE and are not included. In the absence of fresh emissions from ships [*Wonaschuetz et al*., 2013], past measurements in the same study region have suggested that the aerosol is internally mixed in the size range of 150–200 nm [*Hersey et al*., 2009]. Plumes were considered to be a second (internally mixed) aerosol population separate from the background populations [*Modini et al*., 2015]. Figure 1 (top row) shows surface level measurements of aerosol size distribution and chemical composition during E-PEACE.

2.1.2. CIRPAS Twin Otter Flight Measurements

On the CIRPAS Twin Otter, similar instruments as those on the R/V *Point Sur* were used to measure dried aerosol concentrations and properties at various heights (Figure 2). Cloud droplet residuals were sampled with a counterflow virtual impactor (CVI) inlet. Details of this inlet are provided by *Shingler et al*. [2012]. Scanning differential mobility analyzers (models 3081 and 3010, TSI, Inc., St. Paul, MN), with time resolutions of 110 s, and a passive cavity aerosol spectrometer probe (PCASP 0.1–10 μm, PMS Inc., Boulder, Co) were used to measure aerosol size distributions. Multiple CPCs (models 3010 and 3025, TSI, Inc., St. Paul, MN) measured total aerosol concentration. A compact time-of-flight aerosol mass spectrometer (C-ToF-AMS, Aerodyne

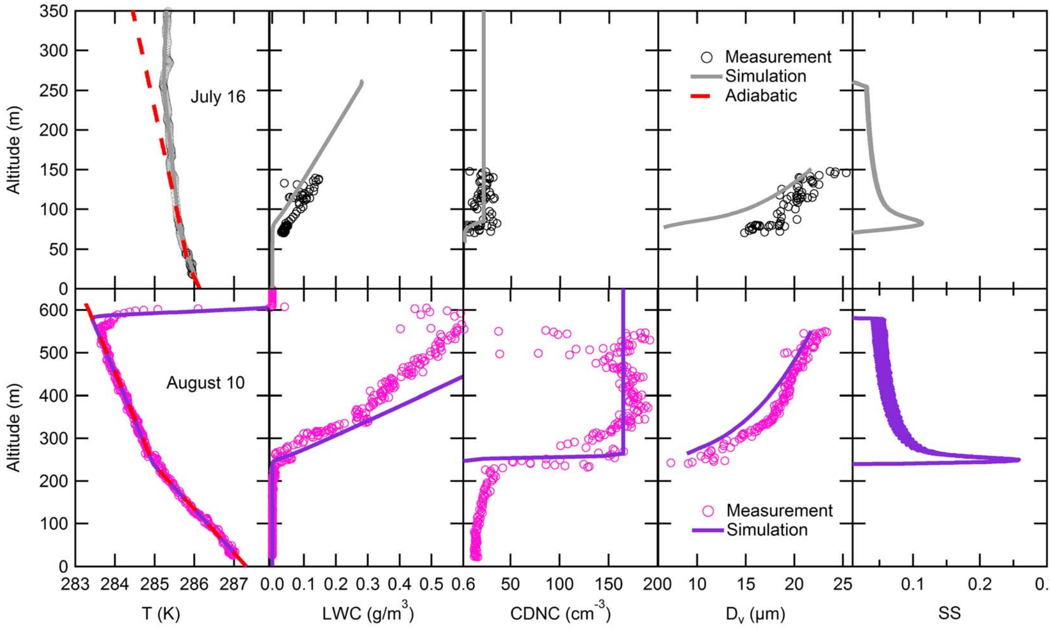

Figure 2. Measured, fitted and simulated profiles of temperature (T), liquid water content (LWC), cloud droplet number concentration (CDNC), volume mean diameter (D_v), and supersaturation (SS) profiles for the CIRPAS Twin Otter flights and ACP model runs for the 10 August and 16 July cases during E-PEACE. The simulations shown are the EJL16B-sa and EAG10B-ad cases from Table 1. For comparison, the adiabatic lapse rate is also shown as a red dashed line. The observations did not include cloud top for 16 July.

Research Inc., Billerica, MA) measured inorganic and organic composition in mass spectrum mode. The C-ToF-AMS had a time resolution of 8–12 s, a size range of 60–600 nm, and a collection efficiency of 0.53 [*Coggon et al.*, 2012]. A CCN counteroperating in scanning flow CCN analysis mode [*Moore and Nenes*, 2009] was used to estimate the maximum supersaturation by comparing the measured CDNC to the CCN at supersaturations between 0.1% and 0.8%. A cloud aerosol spectrometer (CAS) and cloud droplet probe (CDP, DMT, Boulder, CO, [*Lance et al.*, 2010]) measured in-cloud droplet number distributions. *Feingold et al.* [2013] showed that autoconversion and accretion rates are negligible for values of LWC and CDNC that are lower than 0.3 g m^{-3} and 50–200 cm^{-3} (respectively) or 0.5 g m^{-3} and 200–700 cm^{-3} (respectively). Thus, since the values of LWC and CDNC are lower for the case studies used here, droplet number loss by collision coalescence can be neglected. Standard meteorological variables (temperature, wind speed and direction, relative humidity, and pressure) were measured. Relevant cloud measurements are shown in Figure 3, wherein the altitude at which observations were made is compared to model predictions (145 m and 325 m for EJL16 and EAG10), shown in Table 1. Of these measurements, only those within one standard deviation of mean CDNC were averaged to represent the observed droplet distribution to reduce errors in distribution width associated with nonrepresentative (high or low) CDNC. Consequently, for EJL16, 42% and 21% of the measurements in the time series match the background and plume, respectively. For EAG10, 68% and 16% of the measurements in the time series match the criterion used for the background and plume, respectively.

2.2. SOLEDAD

The SOLEDAD campaign consisted of ground-based measurements located near the peak of Mount Soledad, 251 m above sea level, and about 1 km from the Pacific coast. Measurements collected for 49 days (1 May to 18 June 2012) include particle-cloud partitioning of refractory black carbon [*Schroder et al.*, 2014] and salt particle contributions to cloud droplets [*Modini et al.*, 2015]. Measurements on 1 and 13 June 2012 of two cloud events contained sufficient observations for characterizing droplet size and composition of the stratocumulus clouds. Chemical composition and aerosol size distribution (Figure 1) used to initialize the models were collected inside the instrument container; instruments for cloud measurements were mounted on top. We assumed that particle composition was internally mixed and independent of size because size-dependent AMS measurements were below detection limit for the relevant sampling periods and no measurements

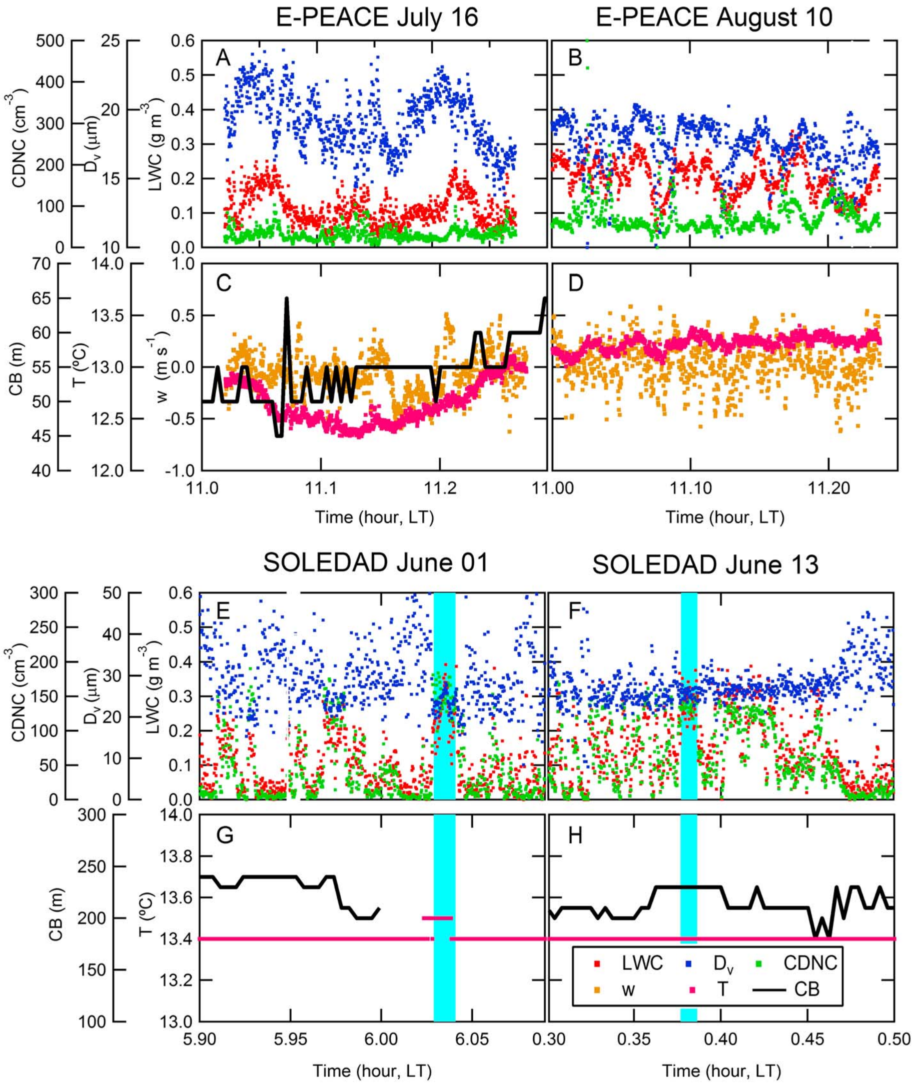

Figure 3. In-cloud measurements of CDNC, LWC, D_V, w, T, and CB for each case. CDP and CAS measured CDNC, D_V, and LWC for E-PEACE 16 July and 10 August cases, respectively. Fog Monitor measurements are used for SOLEDAD CDNC, D_V, and LWC. Cloud base measurements for both SOLEDAD and E-PEACE cases are detected with a ceilometer. Cloud base (CB) measurements for E-PEACE 10 August and vertical velocity measurements for SOLEDAD are not available. Only about 2% of all in-cloud measurements are shown here as these times were identified as consistent conditions for use in initializing the SOLEDAD and E-PEACE cases. Due to the high variability in SOLEDAD cloud measurements, only the cyan-highlighted sections were used for the SOLEDAD cases.

of bulk mixing state were carried out. Two inlets were used to sample ambient aerosols: the high-flow rate isokinetic inlet continuously collected air containing both interstitial aerosols and cloud droplets, and a counterflow virtual impactor (CVI) was used to sample only cloud droplet residuals [*Noone et al.*, 1988; *Schroder et al.*, 2014]. The CVI inlet for droplet residuals was mounted atop the container and was only used during cloud events. During periods with no clouds, all instruments sampled through the isokinetic inlet. Two single-particle soot photometers (SP2, DMT, Boulder, CO) were used to measure refractory black carbon: one continuously measured from the isokinetic inlet and the other measured from the residual inlet during cloud events.

The SEMS measured submicrometer particle number size distributions from the total inlet at all times, while a Scanning Mobility Particle Sizer (SMPS Model 3034, TSI, St. Paul, MN) was used on the CVI inlet during cloud periods and on the total inlet during noncloud periods. The same HR-ToF-AMS used on E-PEACE was used on Mount Soledad to measure aerosol composition on the residual inlet during cloud events to obtain the

Table 1. Observations and ACP Simulation Results

	E-PEACE 16 July Background (EJL16B)	E-PEACE 16 July Smoke Plume (EJL16P)	E-PEACE 10 August Background (EAG10B)	E-PEACE 10 August Cargo Plume (EAG10P)	SOLEDAD 1 June Ambient (SJN01A)	SOLEDAD 13 June Ambient (SJN13A)
Simulation run	ad[a]/al/sa	ad/al/sa	ad/sa	ad/sa	ad/sa	ad/sa
Cloud base (m)	61 ± 9[b]	61 ± 9	240	240	205 ± 23	170 ± 34
	(28)/<70>/<70>	(28)/<70>/<70>	<240>/(295)	<240>/(295)	(160)/(225)	(145)/(200)
Measurement height (m)	145	145	325	325	250	250
Dry lapse rate (K km^{-1})	[−9.8]/[−9.8]/<−7.0>	[−9.8]/[−9.8]/<−7.0>	<−9.8>/[−8.0]	<−9.8>/[−8.0]	[−9.8]/(−7.0)	[−9.8]/(−7.0)
Moist lapse rate (K km^{-1})	-/-/−2.2	-/-/−2.2	−4.5/-	−4.5/-	-	-
	(−4.4)/(−4.4)/<−2.2>	(−4.4)/(−4.4)/<−2.2>	<−4.5>/(−3.4)	<−4.5>/(−3.4)	(−4.1)/(−2.7)	(−4.0)/(−2.8)
Liquid water content (g m^{-3})	–	-/-/0.08 ± 0.08	0.24 ± 0.05/-	0.19 ± 0.06/-	0.25 ± 0.07	0.28 ± 0.04
	(0.34)/(0.24)/(0.11)	(0.34)/(0.24)/(0.09)	(0.25)/(0.08)	(0.25)/(0.08)	(0.28)/(0.06)	(0.32)/(0.10)
Mean D_v (μm)	-/-/19.7 ± 2.0	-/-/18.6 ± 2.0	14.1 ± 1.1/-	12.2 ± 1.1/-	15.5 ± 0.3	16.7 ± 0.2
	(37.2)/(26.8)/(21.0)	(17.7)/(15.3)/(15.2)	(14.0)/(8.8)	(12.1)/(7.9)	(15.5)/(8.8)	(16.8)/(12.6)
Updraft (m s^{-1})	[0.06]	[0.06]	[0.31]	[0.31]	[0.05]	[0.05]
CDNC for a single updraft (cm^{-3})	-/-/21 ± 6	-/-/49 ± 14	156 ± 30/-	277 ± 85/-	148 ± 19	137 ± 8
	(37)/(37)/(22)	(86)/(86)/(50)	(165)/(165)	(241)/(241)	(146)/(108)	(129)/(95)
CDNC for a PDF of updrafts (cm^{-3})	-/-/21 ± 6	-/-/49 ± 14	156 ± 30/-	277 ± 85/-	-	-
	-/-/(23)	-/-/(207)	(160)/-	(296)/-	-	-

[a] The simulation runs use an adiabatic lapse rate with adiabatic cloud base (ad), an adiabatic lapse rate with measured cloud base (al), and a subadiabatic lapse rate with measured cloud base (sa).

[b] Observations (not in brackets) and ACP simulation, inputs from observations <in triangle brackets>, modified inputs [in square brackets], and simulation results (in parentheses).

chemical composition of cloud droplet residuals and on the total inlet during noncloud periods. A fog monitor (FM-100, model 100, DMT, Boulder, CO) was mounted on top of the instrument container to provide cloud in situ measurements of droplet size and concentration, as well as LWC. Figure 3 shows time series of LWC and CDNC for both the SOLEDAD 1 June ambient "A" (SJN01A) case and the 13 June ambient (SJN13A) case. Both LWC and CDNC are highly variable with maximum hourly standard deviations of 0.09 g m^{-3} and 52 cm^{-3} for SJN01A and 0.13 g m^{-3} and 58 cm^{-3} for SJN13A, respectively. The short, cyan-highlighted periods in Figure 3 represent the time periods averaged and compared to model simulations. These time periods were selected because LWC and CDNC were above the detection limit and fairly constant, whereas the remainder of the measurements was quite variable. From the selected time periods, the mean and standard deviation in CDNC were 148 ± 19 cm^{-3} and 137 ± 8 cm^{-3} for the SJN01 and SJN13 cases, respectively. CDNC was within one standard deviation of the subset mean for SJN01 (6.4%) and SJN13 (9.8%), respectively. The measurements were made close to the cloud base. Consequently, small changes in the cloud base height caused large changes in CDNC and LWC. The higher CDNC was chosen because it was more consistent and likely represented the CDNC after maximum supersaturation (Figure S3 in the supporting information).

2.3. Aerosol-Cloud Parcel (ACP) Model

The aerosol dynamics model is based on a fixed-sectional approach to represent the (dry) particle size domain, with internally mixed chemical components and externally mixed types of particles. Using measured aerosol types (or "populations"), the model is described by the number of particles each with an internal mixture of compounds at each size. The model employs a dual moment (number and mass) algorithm to calculate particle growth from one size section to the next for nonevaporating compounds (namely, all components other than water) using an accommodation coefficient of 1.0 [*Raatikainen et al.*, 2013]. The dual moment method is based on *Tzivion et al.* [1987] to allow accurate accounting of both aerosol number and mass. This algorithm incorporates independent calculations of the change in particle number and mass for all processes other than growth. The model includes a dynamic scheme for activation of particles to cloud droplets. Liquid water is treated in a moving section representation, similar to the approach of *Jacobson et al.* [1994], to allow the accurate calculation of evaporation and condensation of water in conditions of varying humidity. In subsaturated conditions, aerosol particles below the cloud base are considered to be in local equilibrium with water vapor. The initial relative humidity at sea level for the simulations ranged from 91% to 98%.

In E-PEACE and SOLEDAD, we assumed that there was no gas-to-particle growth below cloud, so below-cloud condensation was neglected, with the exception of water for which subsaturated liquid vapor equilibrium was assumed. For the relatively short simulations used here (<2 h) at marine concentrations ($<400\ \mathrm{cm}^{-3}$), coagulation, scavenging, and deposition of the aerosol were included in the model but their effects were negligible. The particle size distributions of the background aerosol for the E-PEACE and SOLEDAD cases were modeled as one internally mixed particle type. The plumes were included in the models as separate particle types from the background aerosol. The inorganic ion (NH_4^+, NO_3^-, and SO_4^{2-}) mass fractions measured with the HR-ToF-AMS were apportioned to molecular mass fractions of ammonium nitrate, ammonium sulfate, ammonium bisulfate, sulfuric acid, or nitric acid using the simplified ion pairing scheme of *Gysel et al.* [2007]. Inorganic ion concentrations and molecule concentrations for each case study are in Tables S1 and S2, respectively.

The parcel model is constrained by measured temperature profiles, cloud base height, and updraft velocities whenever available (Figures 2 and 3). The simulations used fixed updraft velocities, based on the calculation that at low updrafts, there is a negligible feedback effect due to small evolved heat of condensation and negligible density and viscosity changes in the nondrizzling air parcel below 500 m. For E-PEACE, vertical profiles of temperature and pressure measured by the CIRPAS Twin Otter were used to provide measured lapse rates. For SOLEDAD, lapse rates were not measured so both adiabatic and subadiabatic conditions were simulated. To account for release of latent heat in the cloud, the vertical temperature gradient was calculated as

$$\mathrm{d}T = -\left(\frac{gw\mathrm{d}t + L\mathrm{d}w_l}{c_p}\right), \tag{1}$$

where $\mathrm{d}T$ is change in temperature, g is acceleration due to gravity, w is updraft velocity, $\mathrm{d}t$ is time step, L is latent heat of water condensation, w_l is liquid water mixing ratio, and c_p is specific heat of water [*Bahadur et al.*, 2012]. A ceilometer (Model CL31, Vaisala) was used to measure cloud base height on the R/V *Point Sur* during E-PEACE and on Scripps Pier (1 km west of the sampling site) during SOLEDAD. Updraft velocities used for E-PEACE simulations were measured on the CIRPAS Twin Otter during E-PEACE; for SOLEDAD, updraft velocities were estimated (as described in section 3.2.1). More detailed model mechanics are given by *Russell and Seinfeld* [1998] and *Russell et al.* [1999].

2.4. GCM Parameterization

The second model used in this study is the parameterization of cloud droplet formation [*Betancourt and Nenes*, 2014; *Fountoukis and Nenes*, 2005; *Nenes and Seinfeld*, 2003] that was designed to be numerically efficient for use in GCMs. It is based on a generalized sectional representation of aerosol size and composition. The parameterization can be used with internally or externally mixed aerosols with size-varying composition, and it can include the effects of surface-active compounds, insoluble compounds, and slightly soluble compounds. The model uses minimal empirical information and is applied in a two-step process. It first accounts for the aerosol number and chemical composition modeled with modified Kohler theory to provide critical supersaturations for each aerosol bin; it next uses an updraft velocity to express a cooling rate and compute the maximum supersaturation using a semianalytical approach. To calculate the condensation rate of water vapor in the supersaturation balance equation, the "population splitting" approach is adopted—which determines the size of droplets at the point of maximum supersaturation in the cloudy updraft. This differential growth of the larger droplets relative to the smaller droplets is important because it affects the estimated surface area for water vapor condensation and supersaturation. Once the maximum supersaturation, s_{max}, is computed, the CDNC is then equal to the CCN with critical supersaturation less than s_{max}. The model takes into account the "inertial" mechanism for kinetic limitation described by *Nenes et al.* [2001], as well as a series of corrections to account for the effects of large particles to preclude errors in maximum supersaturation [*Barahona et al.*, 2010; *Betancourt and Nenes*, 2014]. For a large range of CCN activation conditions, the parameterization does not require empirical information.

2.5. Model Initialization

Both the ACP model and GCM parameterization are initialized by measurements below or before cloud occurrences and are compared to in-cloud measurements from the two field campaigns. The initial and simulated values are provided in Table S3. To initialize the E-PEACE case studies, number concentrations were obtained from merged APS and SMPS measurements on 16 July and from merged scanning differential mobility analyzer (DMA) and PCASP measurements on 10 August. The method described by *Khlystov et al.* [2004] was used to merge the distributions from submicrometer and supermicrometer instruments. Consistent with the available chemical and physical measurements, these simulations were initialized with one internally mixed aerosol population except for the plume cases which consisted of an external mixture of the background (marine) aerosol population and the plume aerosol population. The modeled aerosol chemical constituents are ammonium sulfate, ammonium bisulfate, ammonium nitrate, nitric acid, sulfuric acid, sodium chloride, refractory black carbon, and organic carbon.

Aerosol compositions were obtained from 30 min averaged bulk submicron MS mode HR and C ToF-AMS measurements. Salt concentrations of NaCl were calculated from the components measured by the AMS, scaled by XRF and IC sea-salt concentrations for E-PEACE and SOLEDAD, respectively [*Modini et al.*, 2015]. Sulfate molecules were apportioned using the molar ratio of sulfate to ammonium ions [*Nenes et al.*, 1998]. SP2 measurements, averaged over 5 h, were used for refractory black carbon mass concentrations. Aerosol hygroscopicities as represented by the kappa parameter (κ) were calculated from CCN spectra measurements. Inorganic hygroscopicities (κ_{inorg}) have been measured in laboratory experiments [*Petters and Kreidenweis*, 2007] using the molecular concentrations to then calculate the inorganic contribution to particle hygroscopicity. The organic hygrospopicity (κ_{org}) was then evaluated from the equation

$$\kappa_{\text{measured}} = \kappa_{\text{inorg}}\chi_{\text{inorg}} + \kappa_{\text{org}}\chi_{\text{org}} \tag{2}$$

where χ_{org} and χ_{inorg} are the organic and inorganic volume fractions, respectively. There is uncertainty in the hygroscopicity of the organic fraction because its components are not specific identified molecular compounds and because the hygroscopicity of many organic molecules (or their mixtures) has not been measured [*Petters et al.*, 2015]. For these reasons, we consider a range of values for $\kappa_{\text{org}}X_{\text{org}}$ in different simulations. Refractory black carbon has a hygroscopicity of zero and would have no contribution to the measured hygroscopicity. Finally, meteorological inputs consisted of observed temperature, pressure, and relative humidity profiles were used to initialize the model. The meteorological profiles determined the cloud base temperature and pressure as well as the subsequent forcing on the cloud supersaturation.

2.6. Cloud Reflectivity

Cloud reflectivity (CR) was estimated using the following equation [*Bohren and Battan*, 1980; *Geresdi et al.*, 2006]:

$$\text{CR} = \frac{\left(\sqrt{3}(1-g)\tau\right)}{\left(2+\sqrt{3}(1-g)\tau\right)}, \tag{3}$$

where τ is the cloud optical depth defined as

$$\tau = 2h\text{CDNC}\pi r_e^2; \tag{4}$$

and h is the cloud height or thickness r_e is the cloud effective radius, and g, the asymmetric scattering parameter, is approximated as 0.85 based on Mie scattering calculations for supermicron cloud drops. A CR of 1.0 reflects all visible light, and a CR of 0.0 reflects no visible light.

Cloud reflectivity (CR) is largely dependent on CDNC and cloud droplet size distributions. Cloud droplet effective radius can be approximated as a weighted mean radius of the cloud droplet size distribution

$$r_e = \left(\frac{3\text{LWC}}{4\pi k\text{CDNC}\rho_w}\right), \tag{5}$$

where LWC is liquid water content, ρ_w is density of water, and k is the spectral parameter that represents the reciprocal of the cloud droplet spectrum width [*Hsieh et al.*, 2009]. For example, a monodisperse droplet distribution would have $k = 1$ and a broader droplet distribution is characterized by $k < 1$. The spectral parameter k is calculated as

$$k = \left(\frac{r_v}{r_e}\right)^3, \tag{6}$$

where r_v is the effective volume radius and r_e is the effective radius [*Hsieh et al.*, 2009]. In this manuscript, cloud reflectivity calculations are calculated from cloud base to the measurement height (Table 1) in the cloud and thus do not represent cloud top reflectivity. This approach provides values that are more representative of average cloud properties and avoids the influence of cloud top entrainment.

3. Results

3.1. Initialization of Case Studies

These case studies included six different measured compositions and aerosol size distributions to identify different CCN distributions that initialize the modeled droplet activation. The aerosol composition and aerosol number size distributions with lognormal fits are shown in Figure 1.

Each of the two SOLEDAD cases was internally mixed in one approximately lognormal aerosol mode, which was consistent with a mixture of coastal pollution and sea spray particles suspended in the atmosphere long enough (i.e., "aged") to be internally mixed. The higher concentration of nitrate in cloud than out of cloud shows that secondary aerosol formation from cloud processing contributes to the overall aerosol population. The SJN01A case contained over 50% organics by mass and a concentration of 2290 cm^{-3}. The SOLEDAD 13 June ambient (SJN13A) case was less polluted with 1430 cm^{-3}, a much lower organic mass fraction, and was primarily ammonium sulfate by mass. SJN01A was the only case with a significant amount of refractory black carbon (8% by mass).

The E-PEACE particle number distributions contained multiple modes that were fit to lognormal distributions (Figure 1) and used to initialize the two models. The EJL16B and EAU10B cases had compositions with a large mass fraction of NaCl and lower aerosol number concentrations (160 and 360 cm^{-3}, respectively). The EAG10P contained mostly organic components with sulfuric acid and particle concentrations of 1940 cm^{-3}. The E-PEACE intentionally generated smoke plume case (EJL16P) consisted of nearly 100% organic components with a mean particle concentration of 1790 cm^{-3}. The composition of the E-PEACE background aerosol was modeled as an internally mixed distribution of the chemical compounds (Figure 1). The E-PEACE "background" cases consisted of one particle type, and the "plume" cases had two particle types that represented the generated smoke or cargo ship emissions and the background aerosol.

The vertical temperature profiles for initializing simulations were linear fits of the observed temperatures for the E-PEACE cases (Figure 2). The meteorological profiles determined the cloud base temperature and pressure as well as the subsequent forcing on the cloud supersaturation. The same temperature profile was used for the background and plume cases on each day. The observed temperature profile for EJL16B and EJL16P (on 16 July 2011) was subadiabatic, but the temperature profile for EAU10B and EAU10P (on 10 August 2011) was adiabatic. For the SOLEDAD cases, temperature was only measured at Scripps Pier (14 m ASL) and at the summit (251 m ASL), so the temperature profile below and in cloud was calculated for both adiabatic and subadiabatic conditions. Temperature soundings at airports to the north and south were not consistent with measured surface temperatures at the Mount Soledad site due to local differences and could not be used. Figure 2 also shows LWC, CDNC, and mean volumetric cloud droplet diameter (D_v) for both measurements and simulations of the background cases. The CDNC profile for the EJL16B in Figure 2 stopped at 145 m because the droplet concentration decreased to zero above 145 m, indicating that the Twin Otter aircraft left the cloud. Based on measured lapse rates and observed mean cloud base height, the ACP model reproduced the observed LWC in both E-PEACE cases (Table 1). CDNC increased rapidly in observations and model simulations above cloud base and remained relatively constant throughout the rest of the cloud. The D_v increased with height and agreed well between observations and model simulations, as summarized in Table 1. Table 1 also shows three different simulations for each of the two 16 July E-PEACE cases to illustrate the effect of assuming an adiabatic lapse rate, compared to the observed subadiabatic lapse rate. These are discussed further in section 3.2.1.

3.2. Thermodynamic Constraints on Cloud Droplet Formation, Growth, and Distribution

The ACP model predicted activation and condensational growth of cloud droplets in clouds formed for each case study. In the ACP simulation, the parcel rose vertically at a fixed updraft velocity from the ocean surface to cloud top, with cooling controlled by the measured lapse rate. Changes in updraft velocity due to condensation had negligible effects on drop distributions for the cases studied here, so fixing the updraft velocity had little effect on the predicted drop distribution. The particles took up water and grew in diameter as the relative humidity increased below cloud, sometimes increasing the diameter by a factor of 2 from dry conditions to 90% relative humidity, consistent with measurements [*Wonaschuetz et al.*, 2013]. Differences in droplet number and size relative to equilibrium calculations emerge because faster-growing particles reduce the water vapor available for slower-growing particles. Within the first several meters above the cloud

Table 2. Calculated Sensitivities of CDNC to X_i ($\partial \ln \mathrm{CDNC}/\partial \ln X_i$), Where X_i Is κ_{org}, Γ_d, w, S_{max}, or N_a

	Polluted ($N_a > 1000\ \mathrm{cm}^{-3}$)				Clean ($N_a < 1000\ \mathrm{cm}^{-3}$)	
	EJL16P	EAG10P	SJN01A	SJN13A	EJL16B	EAG10B
κ_{org} (0.05 to 0.20)	0.4	0.10	0	0	0.07	0.05
Γ_d(-7 to $-9.8\ \mathrm{K\ km}^{-1}$)	1.61	0	0.91	.90	1.54	0
W (0.1 to 0.3 $\mathrm{m\ s}^{-1}$)	0.74	0.58	0.60	0.68	0.24	0.51
	16 July (N_a range:160–1790 cm^{-3})			10 August (N_a range: 360–1940 cm−3)		
N_a	0.35			0.34		

base, the particles activate rapidly, and the maximum supersaturation is reached (Figure 2). For the remainder of the in-cloud ascent, activated droplets continued to grow to larger sizes but no additional particles were activated (Figure 2). The detailed measurements of thermodynamic and microphysical properties sufficiently constrain the simulated cloud droplet size distributions to match the mean measured CDNC within 6% and the mean diameter within 10% for five of the six cases (Table 1), thus demonstrating "closure" or consistency of the measured composition with the measured CCN spectra and the inferred and modeled supersaturation.

To understand the role of cloud thermodynamic variability on cloud reflectivity, one can evaluate the sensitivity of each simulated drop distribution to the measured cloud base height (and associated lapse rate) and updraft velocity. CDNC greatly influences cloud reflectivity, and CDNC is sensitive to other variables, such as updraft velocity, aerosol concentration, the hygroscopicity parameter κ, and aerosol distribution parameters [*McFiggans et al.*, 2006; *Reutter et al.*, 2009; *Rissman et al.*, 2004; *Twomey*, 1977]. Table 2 includes CDNC relative sensitivities to aerosol concentration (N_a) and updraft velocity (w), as well as sensitivities to κ_{org}, and the dry lapse rate (Γ_d). The LWC, CDNC, D_v, and CR are shown in Figure 4 as a function of lapse rate, updraft velocity,

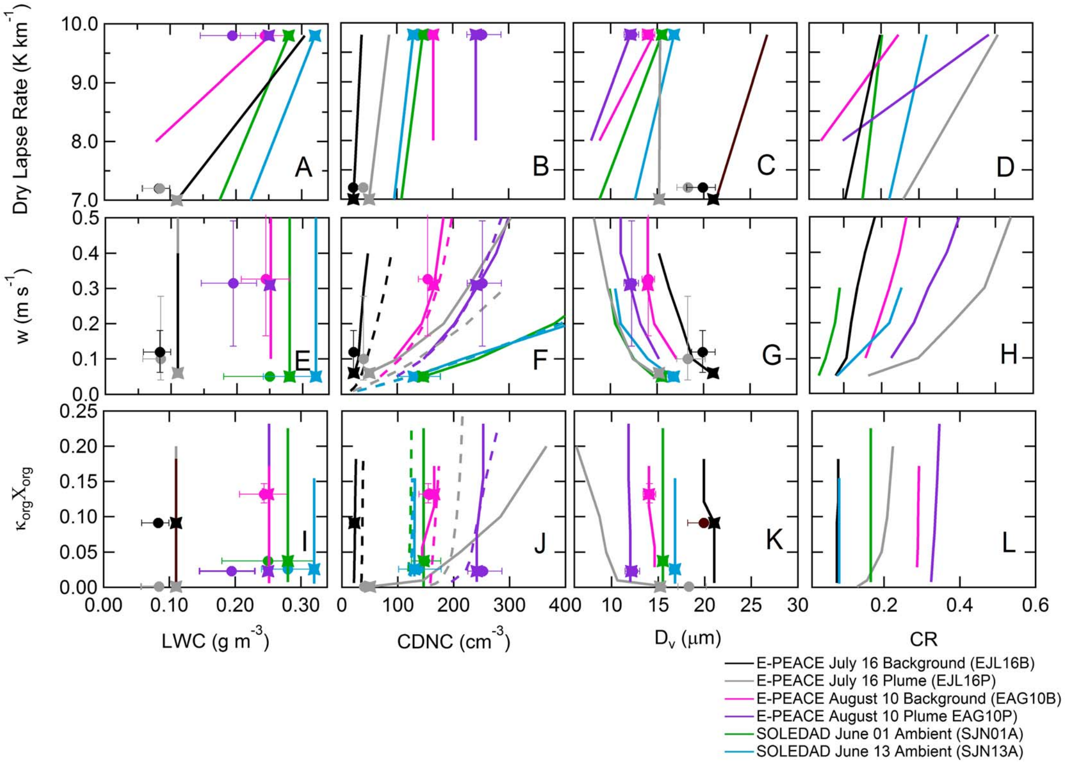

Figure 4. Simulations of LWC, CDNC, D_v, and CR for different values of lapse rate, updraft velocity (w), and organic hygroscopicity ($\kappa_{org}X_{org}$) for the six cases in Table 1. Dashed lines represent the GCM parameterization, and solid lines represent the ACP model. The circles represent the measured 50th quartile, and error bars represent observed 25th and 75th percentiles. The stars represent the simulation runs from Table 1. The $\kappa_{org}X_{org}$ standard deviation is only due to changes in κ_{org} while X_{org} is held constant. Measurements are from the same instruments in Figures 1–3.

and organic hygroscopicity ($\kappa_{\mathrm{org}}X_{\mathrm{org}}$, equation (2)). Error bars in Figure 4 represent 25th and 75th quartiles. SOLEDAD updraft velocities were not measured and are therefore estimated from measurements (this is further explained in section 3.2.1). Lapse rate measurements, organic hygroscopicity ($\kappa_{\mathrm{org}}X_{\mathrm{org}}$) for EAG10P and EJL16P, and updraft velocity for SJN01A and SJN13A have insufficient measurements to define quartiles. The effects of lapse rate and updraft velocity on droplet distribution for the case studies are discussed below.

3.2.1. Variability in Lapse Rate

As a nonentraining air parcel rises through the atmosphere, temperature decreases adiabatically. At the cloud base, the parcel reaches saturation and water condenses and releases latent heat, which decreases the magnitude of the lapse rate. The reduced moist (in-cloud) lapse rate is caused by cooling which also provides additional water for condensation as the parcel rises above the cloud base.

To show the relationship between different lapse rates and cloud base heights, the lapse rate was varied for the subadiabatic E-PEACE cases EJL16P and EJL16B to be adiabatic (Table 1); the other cases were tested with a subadiabatic lapse rate (Table 1). Equation (1) was used to estimate the moist adiabatic lapse rate for E-PEACE cases. SOLEDAD cases used a prescribed lapse rate that resulted in the measured LWC at the height of measurement. To simulate a subadiabatic lapse rate, part of the first term in equation (1), which represents an adiabatic lapse rate of -9.8 K/km (g/c_p), was changed to be subadiabatic (> -9.8 K/km). The measured in-cloud lapse rate (-2.2 K/km) and cloud base height (70 m) are used for EJL16P-sa ("sa" for "subadiabatic lapse rate") and EJL16B-sa cases. These simulations both reproduce measured mean CDNC and LWC within one standard deviation. In EJL16P-al and EJL16B-al (where "al" indicates "adiabatic lapse rate"), the measured cloud base height of 70 m was used but the in-cloud lapse rate was set to be adiabatic (a moist lapse rate of -4.4 K/km as calculated by equation (1)). In both EJL16P-al and EJL16B-al simulations, CDNC and LWC are much larger than measured values. Simulations EJL16P-ad and EJL16B-ad (where "ad" indicates "adiabatic lapse rate and cloud base height") used both the adiabatic cloud base height of 28 m and moist lapse rate of -4.4 K/km. The adiabatic lapse rate simulated a much lower cloud base height, consistent with the findings of *Craven et al.* [2002]. These simulations produced an even larger LWC but similar CDNC as for runs EJL16P-al and EJL16B-al. The simulations also showed that the measured subadiabatic lapse rate, used in simulations EJL16B-sa and EJL16P-sa, caused the parcel of air to reach saturation at a higher altitude and produced a corresponding decrease in the moist lapse rate. This subadiabatic moist lapse rate resulted in lower supersaturations, which caused the measured CDNC and LWC to be lower than that of an adiabatic case. The reduction in CDNC due to subadiabatic lapse rates was consistent with *Leaitch et al.* [1996], who compared the maximum CDNC (associated with parcels having adiabatic lapse rates to the observed average CDNC) and observed CDNC associated with subadiabatic lapse rates for stratocumulus clouds in the North Atlantic. This result also explains why the adiabatic form of the simplified GCM parameterization [*Betancourt et al.*, 2012; *Nenes and Seinfeld*, 2003] produces larger CDNC than was measured for subadiabatic cases (EJL16B-sa and EJL16P-sa), as shown in Figures 4f and 4j. Another reason the *Nenes and Seinfeld* [2003] parameterization does not compare well to the ACP model for the EJL16P case is that this is an unusual case with comparatively high concentrations of large (~1 μm diameter) organic smoke particles. In this case, the empirical data used in the parameterization when CDNC is sensitive to kinetic limitations [*Nenes and Seinfeld*, 2003] were not a good representation of the EJL16P aerosol, specifically of the smoke plume particles. The ACP model and GCM parameterization agree well for the EAG10B-ad and EAG10P-ad cases, largely because the lapse rate measured was adiabatic. However, the GCM parameterization could be adjusted to use a subadiabatic lapse rate. The simulations EAG10B-sa and EAG10P-sa, using a subadiabatic lapse rate of -8 K/km, produced a lower moist lapse rate and resulted in underestimating D_v and LWC. A subadiabatic lapse rate of -7 K/km could not be used to compare to measurements for the 10 August cases because it led to cloud formation above the observed cloud base height. These subadiabatic cases had the same CDNC as the "al" case. This result differs from the other cases because the lapse rate is closer to adiabatic and because the updraft velocity is higher. Figure 4f shows that CDNC is less sensitive at higher updraft velocities, as seen in *Rissman et al.* [2004]. The SOLEDAD cases used simulated updraft velocity and lapse rate because there were no measured updraft velocities or meteorological profiles. This information was estimated with the ACP model by matching the simulated results of LWC and CDNC to the observed values. The results from a pure adiabatic lapse rate and a subadiabatic lapse rate of -7 K/km were simulated and are also shown in Table 1. For both SOLEDAD cases, the simulations with subadiabatic lapse rate predicted fewer cloud droplets and less LWC than simulations with an adiabatic lapse rate, similar to the E-PEACE cases. CDNC is most sensitive to changes

Table 3. Observed and Simulated Spectral Parameter (*k*)

	E-PEACE 16 July Background (EJL16B)	E-PEACE 16 July Smoke Plume (EJL16P)	E-PEACE 10 August Background (EAG10B)	E-PEACE 10 August Cargo Plume (EAG10P)	SOLEDAD 1 June Ambient (SJN01A)	SOLEDAD 13 June Ambient (SJN13A)
Observations	0.84 ± 0.05	0.87 ± 0.04	0.90 ± 0.03	0.93 ± 0.02	0.71 ± 0.03	0.72 ± 0.01
Simulations single updraft velocity	0.98	0.98	1.00	1.00	0.72	0.89
PDF of updraft velocities	0.96	0.87	0.96	0.93	-	-
PDF of cloud bases	0.98	0.96	0.97	0.96	0.62	0.81
PDF of updraft velocities and cloud bases	0.89	0.81	0.93	0.87	-	-

in lapse rate for the EJL16P, EJL16B, SJN01A, and SJN13A cases as shown in Table 3. The remaining cases, EAG10P and EAG10B, show no sensitivity to lapse rate possibly due to the low aerosol bin resolution.

The subadiabatic lapse rates may result from mixing. Cloud top entrainment can cause deviations from the moist adiabatic profile, but typically, those effects are most evident close to the top of the cloud [*Nicholls and Leighton*, 1986]. The subadiabatic temperature profile in the cases shown here extends to below cloud base. Also, the clouds were only simulated up to the measurement heights, which were several tens of meters below the cloud top, so that cloud top effects were likely minimal. Therefore, effects of cloud top entrainment are small but the reflectivity is biased slightly low.

In Figures 4a–4d, different simulated lapse rates are shown to vary CDNC, LWC, and CR. The reasons for these dependencies are the same as in the previous paragraph. Variation of CDNC and LWC cause variation in D_v (Figure 4c) and CR (Figure 4d). Measurements from SOLEDAD were taken close to cloud base at an average of 45 m and 80 m above cloud base for SJN01A and SJN13A, respectively. LWC and CDNC correlated well on both days (Figure S3), which further suggests that measurements were taken near cloud base because, as shown in Figure 2 for EJL16B and EAG10B, CDNC quickly reached its maximum value above cloud base. It is possible that the decreased cooling rate was caused by a subadiabatic lapse rate, leading to a decrease in CDNC. The subadiabatic cases for both SOLEDAD cases (Table 1) had simulated LWC and CDNC that were within one standard deviation of observations for 6% of all in-cloud droplet measurements, consistent with subadiabatic lapse rates. E-PEACE cases had a much smaller variation in number concentration (Figure 3); however, they had significant variations in LWC and cloud base height. To identify the effect of LWC variation due to lapse rate variation, a probability distribution function (PDF) of measured cloud base heights (Figure S5) was used in the ACP model to estimate *k* (Table 3). Variability in cloud base height (or lapse rate) alone broadens the cloud droplet distribution, but it is still narrower than observed for all cases with the exception of the SJN01A case (Table 3 and Figure 5). Table 3 shows that four of the six cases are estimated to have droplet spectral widths within observed error when using a distribution of updrafts or cloud base heights rather than a single updraft and cloud base height. The SJL13A case does not have updraft measurements, so variability in *k* with cloud base height could not be calculated. The SJL01A case had a simulated *k* value from a single updraft and cloud base height that was within 2% of the observed *k* value. The SJL01A case had measurements close to cloud base where supersaturation is at maximum. *Hsieh et al*. [2009] found that the *k* value at the height of maximum supersaturation is a good representation of the *k* value throughout the cloud; therefore, that constant updraft simulation *k* is comparable to observations for SJL01A, consistent with the result of *Hsieh et al*. [2009].

3.2.2. Variability in Updraft Velocity

Variations in updraft velocity have the potential to broaden the cloud droplet distribution. Updraft velocity controls the maximum supersaturation, which in turn determines the smallest (and least hygroscopic) particles that can activate. In fast updrafts, there is less time available for water vapor uptake by aerosols, which causes higher supersaturation and activation of more particles. CDNC increases with updraft velocity, as shown in Figure 4f. As noted by *Chuang* [2006] and *McFiggans et al*. [2006], CDNC is more sensitive to updraft velocity variation in polluted cases (Table 2). Updraft velocity also affects droplet size (D_v in Figure 4g) as a consequence of increased CDNC for a given constant LWC.

Since updraft velocity affects CDNC (and, for constant LWC, drop size), variability in updraft velocity results in broadening of the observed cloud drop distribution. Simulated cloud droplet distributions always produce narrower droplet distributions (larger *k*) than measured when applying a constant updraft and lapse rate.

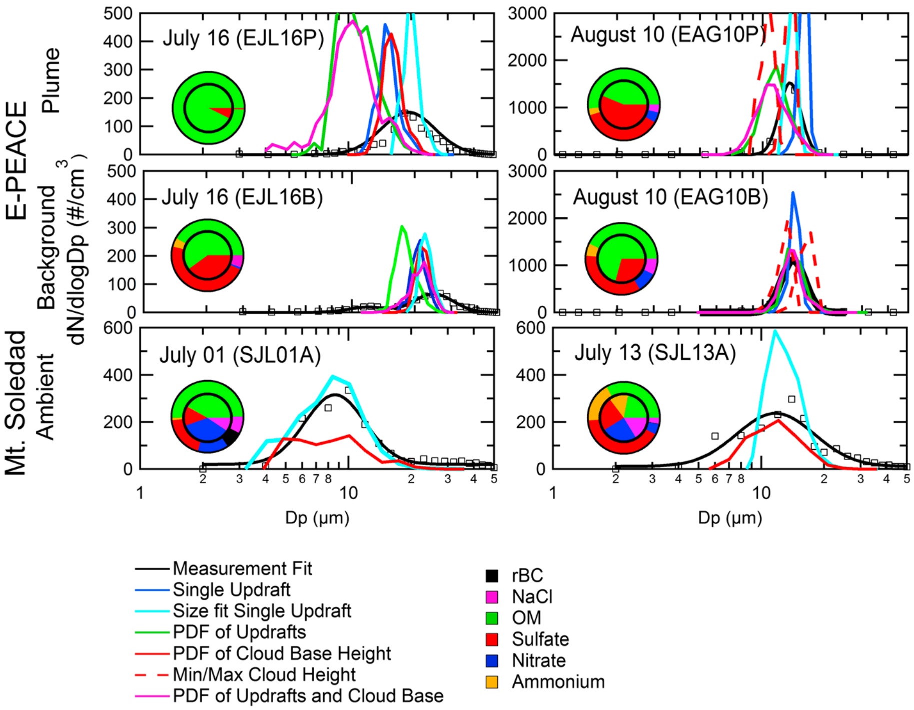

Figure 5. Cloud droplet size distributions are presented for the cases in Table 1. Each case contains cloud droplet distribution measurements as black squares with a lognormal fit. Blue distributions are simulation results based on a single updraft (constrained by CCN spectra behind the CVI, equivalent to the measured CDNC). Light blue distributions also use the same single updraft velocity; however, the cloud base in the simulation is adjusted so the peak measured fits correspond to simulation peaks. Green and solid red distributions are simulation results for a probability distribution of updrafts and cloud base, respectively. Dashed red distributions simulated droplet distributions using minimum and maximum measured cloud base heights for cases without ceilometer measurements. Finally, magenta distributions are simulation results for the combined probability distribution of updrafts and cloud base heights. The inner pie represents the simulated composition, and the outer pie represents the measured composition.

Figure 5 consists of droplet size distributions from the ACP model for each case, as well as the observed cloud droplet distribution. Figure 5 shows that using an ensemble of updrafts instead of a single updraft to simulate observed *k* values is better at reproducing the droplet spectral parameter *k* than a single updraft, which agrees with the findings of *Hsieh et al.* [2009]. Since the SOLEDAD cases did not include vertical velocity measurements, it was not possible to include a droplet distribution using a PDF of measured updraft velocities. The simulated distribution with a single updraft velocity for SJL01A in Figure 5 matched the observed droplet distribution width well, unlike the other cases. This is possibly because the measurements were close to cloud base, and the broadening of the droplet distributions due to variations in updraft velocity and lapse rate at cloud base is not significant till higher altitudes.

3.2.3. Combined Variability of Cloud Base Height (Lapse Rate) and Updraft Velocity

We have shown that updraft velocity variability and cloud base height variability both increase droplet distribution width (decrease *k*). However, using either a distribution of cloud base heights or updraft velocities, but not both, is not sufficient to broaden the distribution of *k* values to observed values for the E-PEACE background cases (Table 3). By incorporating variability of both cloud base height and updraft velocity, the simulated droplet distributions best approximate the observed distributions and spectral parameter for background cases. The combined influence of both variables on the distribution width creates a broader distribution than when each is considered separately. Simulated E-PEACE plume cases have distributions broader than those observed. It is possible that the measured updraft velocity and cloud base height distributions are not representative because the small horizontal area may include only a subset of the measured updraft distribution. *Chuang* [2006] showed that in polluted cases small variations in the updraft velocity can cause large variations in CDNC. For the EJL16P case, for example, the distribution of updrafts produced a simulated CDNC that exceeded the measured values by a factor of 3. However, for all other cases a distribution of updrafts produced CDNC within one standard deviation of the measured CDNC.

3.3. Effects of Organic Composition and Hygroscopicity on Cloud Droplet Formation, Growth, and Distributions

Aerosol hygroscopicity can also play a role in determining CDNC [*Petters and Kreidenweis*, 2007]. Figure 5 shows in-cloud droplet composition as measured and simulated (inner and outer circles, respectively) in the cloud. The inorganic and organic fractions of the measured and simulated compositions are of roughly similar magnitude, but noticeable differences exist in each case. In-cloud aqueous uptake or production of sulfate, nitrate, and organic compounds can explain discrepancies between predicted and measured composition [*Charlson et al.*, 1987; *Hayden et al.*, 2008; *Modini et al.*, 2015; *Prabhakar et al.*, 2014; *Sorooshian et al.*, 2013, 2015; *Youn et al.*, 2015]. The lack of gas phase measurements precludes a detailed analysis; however, we note that during E-PEACE Twin Otter cloud droplet residual particle measurements, downstream of the CVI, suggest dissolution of precursor vapors and in-cloud production of such compounds [*Prabhakar et al.*, 2014; *Sorooshian et al.*, 2013, 2015; *Youn et al.*, 2015].

Organic aerosol component hygroscopicity has been shown to have a small effect on CDNC in nonpolluted situations [*Dusek et al.*, 2006], whereas in polluted cases CDNC can be strongly affected [*Hegg et al.*, 2010; *Twohy et al.*, 2013]. To investigate the sensitivity of CDNC to the organic component, the GCM parameterization and ACP model were initialized with a range of typically observed κ_{org} values (0.01–0.3). These were multiplied by the organic aerosol volumetric fraction to obtain the hygroscopicity due to organics ($\kappa_{org}X_{org}$, Figures 4i–4l). The CDNC sensitivity to κ_{org} is largest for the EJL16P and EAG10P cases (Figure 4j and Table 2). All of the calculated sensitivity values to κ_{org} are all smaller than κ sensitivities reported by *Reutter et al.* [2009], likely because κ_{org} represents only a small fraction of the total κ. The only exception is the EJL16P case, which consists entirely of organic components, such that $\kappa_{org} = \kappa$. The plume cases exhibit the largest effect because of a high organic volume fraction, a high aerosol concentration, and the largest degree of external mixing from the background aerosol. EJL16P, for which the aerosol was entirely organic (Figure 1), showed the greatest change in simulated CDNC (increasing by a factor of 6) with organic hygroscopicity. EAG10P exhibited the second greatest increase in CDNC at 34%. Background aerosol organic hygroscopicity has little effect on CDNC, with an increase of only 17% and 10% over the tested κ_{org} range for EJL16B and EAG10B, respectively, because the background aerosols were mostly inorganic and internally mixed. The highly hygroscopic salt and sulfate particles produce high total hygroscopicity, even when the organic hygroscopicity is low, because the organic volume fraction itself was low. High aerosol hygroscopicity caused rapid uptake of water, preventing further activation of droplets despite increases in organic hygroscopicity [*Modini et al.*, 2015]. The variation in CDNC due to κ_{org} significantly affects other cloud properties such as D_v and CR (Figures 4i–4l). *Ervens et al.* [2010] found that different assumptions for organic solubility and mixing state for marine conditions often lead to similar CDNCs, so reasonable closure could be achieved with assumptions that were not representative of the actual aerosol composition. This is in agreement with our results for the ambient background cases in which the organic hygroscopicity has little effect on the CDNC. Results from *VanReken et al.* [2003] show that closure was observed within 20% with the broad assumption that all the aerosol was composed entirely of ammonium sulfate, indicating that in the cases they studied the CDNC is not very sensitive to even the total hygroscopicity of marine aerosols. External mixtures are necessary for the plume cases because assuming a completely internally mixed aerosol population was shown to overestimate droplet concentration in polluted conditions where there is a greater fraction of less hygroscopic aerosol [*West et al.*, 2014].

The organic composition and hygroscopicity are important if the organic volume fraction is sufficiently large and mainly externally mixed. κ_{org} does not have a strong influence on changes in CDNC for background cases because of low concentrations just below critical diameters. CDNC is not predicted to increase much in the background cases; the change in critical diameter for all cases was 5 nm or less for an increase in κ_{org} of 0.1, except for EJL16P. In fact, the EJL16B case exhibited the largest change in critical diameter (5 nm), for an increase in κ_{org} of 0.1, even though CDNC increased the least in the E-PEACE cases. In terms of the effect of κ_{org} on CDNC, the CDNC can increase only as much as the concentration between the two critical diameters representing the two different κ_{org} values (Figure S4). To test the effect of aerosol concentrations in this narrow size range (marked on Figure S4) on CDNC, the bin concentrations were changed to be a fraction of the measured value for size bins below the critical diameter for $\kappa_{org} = 0.01$. Figure 6 illustrates how aerosol number concentration between the critical diameters (indicated in Figure S4) is essential in understanding the effect κ_{org} can have on CDNC. In Figure 6 (top), the EAG10P case represents the maximum concentration

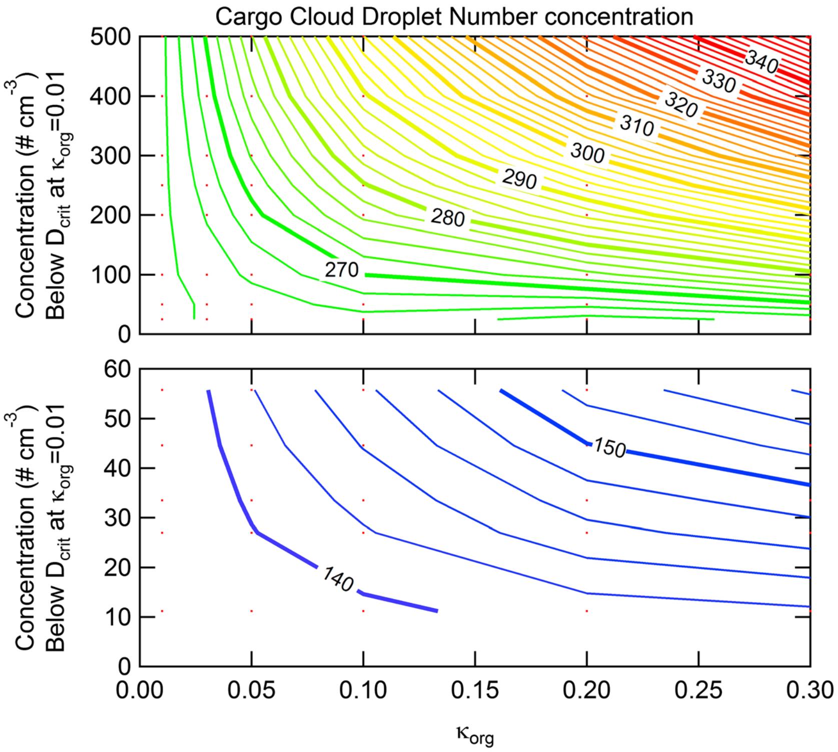

Figure 6. (top) Simulated cloud droplet number concentrations for 10 August cargo ship plume and (bottom) background are shown as a function of κ_{org} and concentration in bins below critical diameter when $\kappa_{org} = 0.01$. Red dots indicate the combination of κ_{org} and concentration in bins below critical diameter for each simulation.

presented, while the lowest concentration represents a 95% decrease in the subcritical diameter concentration at a κ_{org} of 0.01. Figure 6 (top) illustrates that an increase in CDNC due to a change in κ_{org} is largely dependent on the concentration between the two critical diameters associated with the two κ_{org} values, as shown in Figure S4. Figure 6 (bottom) represents the EAG10B case. The change in CDNC with κ_{org} is also shown to decrease with a below critical diameter concentration at a κ_{org} of 0.01. From overall concentrations tested in Figure 6 (bottom), the change in CDNC is much smaller than in the plume case (Figure 6, top) because there are fewer particles in the bins below the critical diameter. This suggests that κ_{org} is most influential on CDNC for plumes or polluted areas in which the critical diameter falls near the peak of an aerosol mode.

In the two E-PEACE background cases and two SOLEDAD ambient cases, the uncertainty and variability in organic composition and hygroscopity are unlikely to contribute significantly to differences between the measured and simulated droplet number distribution (and its spectral width, *k*) or the droplet concentration. The organic fraction was largest in plume sources, wherein organic hygroscopicity exhibits a larger effect than in background and ambient aerosol cases. Furthermore, the low aerosol concentrations in the background cases were such that changes in hygroscopicity have little effect on droplet concentration. Even with high aerosol concentrations, such as in the ambient SOLEDAD cases where the inorganic fraction is high and the inorganic contribution to the aerosol hygroscopicity is much larger than the organic contribution, any change in organic hygroscopicity had no significant effect on CDNC and size.

3.4. Impacts of Thermodynamic and Composition Properties on Cloud Reflectivity

Updraft velocity, organic aerosol hygroscopicity, and lapse rate can affect CDNC and LWC, both of which influence ultimate CR. CR calculations were completed for each case corresponding to variations in κ_{org} and *k*. Spectral parameter comparisons were calculated from a single ACP model run with one updraft velocity, several model runs from a PDF of updrafts, a PDF of cloud base heights, and the *k* value of measured distributions (Table 3). For all cases, droplets above 2 μm in diameter were used to calculate *k* except for the EJL16P case. In the EJL16P only droplets above 5 μm in diameter were used to calculate *k* because some aerosol particles exceeded 2 μm but did not activate and were not counted as cloud droplets.

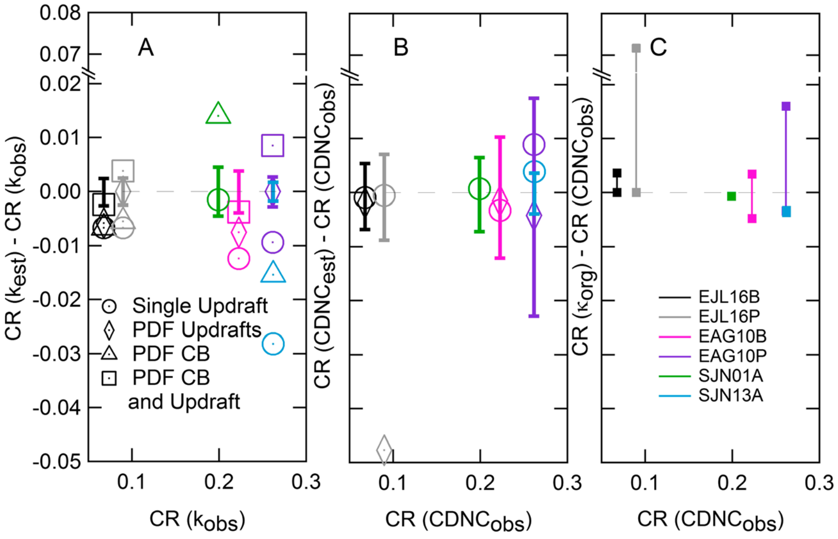

Figure 7. Calculated cloud reflectivity (CR) (a) as a function of the spectral parameter (k) using the observed CDNC and (b) as a function of CDNC using the observed k. Error bars represent the CR as a function of k_{obs} ± one standard deviation (Figure 7a) and $CDNC_{obs}$ ± one standard deviation (Figure 7b). (c) CR is calculated as a function of κ_{org} (κ_{org} values of 0.01 and 0.3 shown as higher and lower CR, respectively) using the observed k. CR was unaffected by κ_{org} for the SJN01A and SJN13A cases, resulting in a single point instead of a range. Each case is represented by the same colors as in Figure 4.

k values are mainly constant in model predictions and observations, with the exception of those near cloud base where particles activate and their classification as droplet or interstitial is ambiguous. The SOLEDAD measurements were carried out near cloud base, which is thought to be why the observed spectral parameter k was lower than in the E-PEACE cases (Table 3).

Applying a PDF of updrafts and cloud base heights (due to variable lapse rates) instead of a single value improves the agreement between observed and simulated k and improves CR estimates. Applying a PDF of updrafts and cloud base heights also affects CDNC, even though it can be modeled well with a single updraft and cloud base height. To observe the influence of k and CDNC separately, in Figure 7a we used the observed CDNC and simulated k to calculate CR; in Figure 7b, we used the simulated CDNC and observed k. Error bars in each plot express one standard deviation of the observed CDNC or k. As shown in Figure 7b, all cases lie within the error bars, except the EJL16P case because CDNC is highly sensitive to updraft velocity. When the CR is a function of k, many cases lie outside the error bars. The influence of k on CR can also be compared to the κ_{org} effect on CR (Figure 7c). With the exception of the two plume cases, the change in CR for κ_{org} from 0.01 to 0.3 is much smaller than the effect of the simulated range of k on CR. Overall, the use of a distribution of updrafts and lapse rates broadened the droplet spectral width, reducing differences between observed and simulated CR, with the exception of the SJL01A, in which measurements were close to cloud base [*Hsieh et al.*, 2009].

4. Conclusions

This work presents a comparison of predictions of two models of aerosol activation and subsequent cloud droplet evolution with measurements from two field studies carried out over the Pacific Ocean off the coast of California and on the California Pacific coast, E-PEACE in 2011 and SOLEDAD in 2012. One model is a comprehensive size-resolved aerosol-cloud parcel model (ACP), and the second is a global climate model (GCM) parameterization of aerosol activation and cloud formation. Four aerosol cases were analyzed from E-PEACE: a generated organic smoke plume, a cargo ship plume, and two cases of background marine aerosols. The two SOLEDAD cases had aerosol compositions and concentrations characteristic of polluted marine conditions. The model was initialized with aerosol composition taken from HR-ToF-AMS and size distribution measurements. Vertical profiles of meteorological parameters and aerosol size distributions were also used as model inputs. Four of the cases were characterized by a subadiabatic lapse rate, which led to fewer droplets owing to decreased maximum supersaturation, lower LWC, and higher cloud base height. Such comparisons are important in order to assess the extent to which models can replicate actual atmospheric conditions. Predictions of cloud microphysical properties depend on a number of key variables, including ambient lapse rate, aerosol size distribution, chemical composition, and updraft velocity; the lack of agreement between predictions and observations often reveals uncertainties in the governing physical processes because these variables are not sufficiently constrained by measurements.

For the E-PEACE cases, a weighted ensemble of simulations that reflect the measured variation in updraft velocity and cloud base height reproduced the observed droplet distributions within 9%, excluding the case of the generated organic smoke plume. Vertical velocity was not measured in SOLEDAD, so an estimated updraft of $0.05\ \mathrm{m\,s^{-1}}$ was used (reproducing CDNC observations with errors of 1% and 6%). A distribution of cloud base heights and updraft velocities produced simulations with a broader cloud droplet distribution than achieved using a single updraft or cloud base height.

In comparing simulated and measured cloud droplet composition, differences suggest a possible role of in-cloud uptake or production of sulfate, nitrate, and organic components. To examine the CDNC sensitivity to the aerosol organic fraction, simulations were initialized with a range of organic hygroscopicities (Table 2). The organic fraction in marine background aerosols tends to be too low for organic hygroscopicity to affect CDNC because background particles contain internally mixed hygroscopic salts. However, generated smoke and cargo ship plume aerosols, which have a substantial organic fraction and a large aerosol concentration near the critical diameter of cloud active aerosol, exert a large effect on CDNC. CDNC in such plumes is strongly dependent on the value of the aerosol hygroscopicity, $\kappa_{\mathrm{org}}X_{\mathrm{org}}$, due to both the high organic fraction and aerosol concentration. $\kappa_{\mathrm{org}}X_{\mathrm{org}}$ in the SOLEDAD experiment showed no effect on CDNC, even at the high aerosol concentrations present, because the prevalent inorganic hygroscopic fraction dominates cloud activation. To explore the role of aerosol size and its combined effect with $\kappa_{\mathrm{org}}X_{\mathrm{org}}$, we varied the aerosol concentration in the size bin(s) just below the critical diameters to show that an increase in CDNC, due to a change in $\kappa_{\mathrm{org}}X_{\mathrm{org}}$, is largely dependent on the difference in concentration near the critical diameters. In other words, $\kappa_{\mathrm{org}}X_{\mathrm{org}}$ has the strongest influence on CDNC when the critical diameter falls near the peak of an aerosol mode.

In addition, droplet size, CDNC, and droplet distribution width (k) affect cloud reflectivity (CR). Changes in organic hygroscopicity are found to have little or no effect on CR, with the exception of a case with a fresh smoke plume (EJL16P; section 3.4), in which CDNC increased by a factor of 6 (to $300\ \mathrm{cm}{-3}$ from $49\ \mathrm{cm}^{-3}$), causing an increase in CR from 0.09 to 0.16 (where a CR of 1.0 reflects all visible light), due to its high fraction of externally mixed organics. A case with a cargo ship plume (EAG10P; section 3.4) had the second greatest increase in CDNC with increasing κ_{org}. However, the cloud droplet concentration was already high ($277\ \mathrm{cm}^{-3}$) compared to other cases so the increase in CDNC of 35% had little effect on CR, increasing it from 0.26 to 0.28. The difference in cloud k values caused a change in CR ranging from ~0.01 to 0.03 for all cases, when the CDNC is equal to the observed value, while organic hygroscopicity caused a difference of <0.01 in CR for the cases without fresh plumes.

Acknowledgments

This work was funded by NSF AGS-1013423, NSF AGS-1360645, NSF AGS-1008848, DOE DE-SC0006679, ONR grants N00014-11-1-0783, N00014-10-1-0200, and N00014-10-1-0811, and EC Finance ID 1300359. Kevin J. Sanchez appreciates the support of the San Diego Foundation. We gratefully acknowledge the help and support of the crew and staff of the R/V *Point Sur* and the CIRPAS Twin Otter, as well as assistance from Bill Shull and Ken Duff of Scripps Institution of Oceanography. Finally, we thank Bruce Albrecht for the ceilometer measurements taken on both the SOLEDAD and E-PEACE campaigns. Corresponding data can be found at https://library.ucsd.edu/dc/object/bb2391869d.

References

Allan, J. D., et al. (2009), Composition and properties of atmospheric particles in the eastern Atlantic and impacts on gas phase uptake rates, *Atmos. Chem. Phys.*, *9*(23), 9299–9314.

Bahadur, R., L. M. Russell, M. Z. Jacobson, K. Prather, A. Nenes, P. Adams, and J. H. Seinfeld (2012), Importance of composition and hygroscopicity of BC particles to the effect of BC mitigation on cloud properties: Application to California conditions, *J. Geophys. Res.*, *117*, D09204, doi:10.1029/2011JD017265.

Barahona, D., R. E. L. West, P. Stier, S. Romakkaniemi, H. Kokkola, and A. Nenes (2010), Comprehensively accounting for the effect of giant CCN in cloud activation parameterizations, *Atmos. Chem. Phys.*, *10*(5), 2467–2473.

Betancourt, R. M., and A. Nenes (2014), Droplet activation parameterization: The population-splitting concept revisited, *Geosci. Model Dev.*, *7*(5), 2345–2357, doi:10.5194/gmd-7-2345-2014.

Betancourt, R. M., D. Lee, L. Oreopoulos, Y. C. Sud, D. Barahona, and A. Nenes (2012), Sensitivity of cirrus and mixed-phase clouds to the ice nuclei spectra in McRAS-AC: Single column model simulations, *Atmos. Chem. Phys.*, *12*(22), 10,679–10,692, doi:10.5194/acp-12-10679-2012.

Bohren, C. F., and L. J. Battan (1980), Radar backscattering by inhomogeneous precipitation particles, *J. Atmos. Sci.*, *37*(8), 1821–1827, doi:10.1175/1520-0469(1980)037<1821:rbbipp>2.0.co;2.

Charlson, R. J., J. E. Lovelock, M. O. Andreae, and S. G. Warren (1987), Oceanic phytoplankton, atmospheric sulfur, cloud albedo and climate, *Nature*, *326*(6114), 655–661, doi:10.1038/326655a0.

Chuang, P. Y. (2006), Sensitivity of cloud condensation nuclei activation processes to kinetic parameters, *J. Geophys. Res.*, *111*, D09201, doi:10.1029/2005JD006529.

Coggon, M. M., et al. (2012), Ship impacts on the marine atmosphere: Insights into the contribution of shipping emissions to the properties of marine aerosol and clouds, *Atmos. Chem. Phys.*, *12*(18), 8439–8458, doi:10.5194/acp-12-8439-2012.

Collins, D. B., et al. (2013), Impact of marine biogeochemistry on the chemical mixing state and cloud forming ability of nascent sea spray aerosol, *J. Geophys. Res. Atmos.*, *118*, 8553–8565, doi:10.1002/jgrd.50598.

Conant, W. C., et al. (2004), Aerosol-cloud drop concentration closure in warm cumulus, *J. Geophys. Res.*, *109*, D13204, doi:10.1029/2003JD004324.

Craven, J. P., R. E. Jewell, and H. E. Brooks (2002), Comparison between observed convective cloud-base heights and lifting condensation level for two different lifted parcels, *Weather Forecasting*, *17*(4), 885–890, doi:10.1175/1520-0434(2002)017<0885:cboccb>2.0.co;2.

Cruz, C. N., and S. N. Pandis (1997), A study of the ability of pure secondary organic aerosol to act as cloud condensation nuclei, *Atmos. Environ.*, *31*(15), 2205–2214, doi:10.1016/s1352-2310(97)00054-x.

Cruz, C. N., and S. N. Pandis (2000), Deliquescence and hygroscopic growth of mixed inorganic-organic atmospheric aerosol, *Environ. Sci. Technol.*, *34*(20), 4313–4319, doi:10.1021/es9907109.

DeCarlo, P. F., et al. (2006), Field-deployable, high-resolution, time-of-flight aerosol mass spectrometer, *Anal. Chem.*, *78*(24), 8281–8289, doi:10.1021/ac061249n.

Dusek, U., et al. (2006), Size matters more than chemistry for cloud-nucleating ability of aerosol particles, *Science*, *312*(5778), 1375–1378, doi:10.1126/science.1125261.

Ervens, B., et al. (2010), CCN predictions using simplified assumptions of organic aerosol composition and mixing state: A synthesis from six different locations, *Atmos. Chem. Phys.*, *10*(10), 4795–4807, doi:10.5194/acp-10-4795-2010.

Facchini, M. C., et al. (2008), Primary submicron marine aerosol dominated by insoluble organic colloids and aggregates, *Geophys. Res. Lett.*, *35*, L17814, doi:10.1029/2008GL034210.

Feingold, G., A. McComiskey, D. Rosenfeld, and A. Sorooshian (2013), On the relationship between cloud contact time and precipitation susceptibility to aerosol, *J. Geophys. Res. Atmos.*, *118*, 10,544–10,554, doi:10.1002/jgrd.50819.

Fountoukis, C., and A. Nenes (2005), Continued development of a cloud droplet formation parameterization for global climate models, *J. Geophys. Res.*, *110*, D11212, doi:10.1029/2004JD005591.

Frossard, A. A. (2014), Investigation of the sources and composition of submicron organic aerosol particles in marine environments through artificial generation and atmospheric measurements, PhD thesis, 243 pp., Univ. of Calif., San Diego.

Geresdi, I., E. Meszaros, and A. Molnar (2006), The effect of chemical composition and size distribution of aerosol particles on droplet formation and albedo of stratocumulus clouds, *Atmos. Environ.*, *40*(10), 1845–1855, doi:10.1016/j.atmosenv.2005.11.012.

Gysel, M., J. Crosier, D. O. Topping, J. D. Whitehead, K. N. Bower, M. J. Cubison, P. I. Williams, M. J. Flynn, G. B. McFiggans, and H. Coe (2007), Closure study between chemical composition and hygroscopic growth of aerosol particles during TORCH2, *Atmos. Chem. Phys.*, *7*(24), 6131–6144.

Hawkins, L. N., L. M. Russell, D. S. Covert, P. K. Quinn, and T. S. Bates (2010), Carboxylic acids, sulfates, and organosulfates in processed continental organic aerosol over the southeast Pacific Ocean during VOCALS-REx 2008, *J. Geophys. Res.*, *115*, D13201, doi:10.1029/2009JD013276.

Hayden, K. L., A. M. Macdonald, W. Gong, D. Toom-Sauntry, K. G. Anlauf, A. Leithead, S. M. Li, W. R. Leaitch, and K. Noone (2008), Cloud processing of nitrate, *J. Geophys. Res.*, *113*, D18201, doi:10.1029/2007JD009732.

Healy, R. M., et al. (2014), Predicting hygroscopic growth using single particle chemical composition estimates, *J. Geophys. Res. Atmos.*, *119*, 9567–9577, doi:10.1002/2014JD021888.

Hegg, D. A., D. S. Covert, H. H. Jonsson, and R. K. Woods (2010), The contribution of anthropogenic aerosols to aerosol light-scattering and CCN activity in the California coastal zone, *Atmos. Chem. Phys.*, *10*(15), 7341–7351, doi:10.5194/acp-10-7341-2010.

Hersey, S. P., A. Sorooshian, S. M. Murphy, R. C. Flagan, and J. H. Seinfeld (2009), Aerosol hygroscopicity in the marine atmosphere: A closure study using high-time-resolution, multiple-RH DASH-SP and size-resolved C-ToF-AMS data, *Atmos. Chem. Phys.*, *9*(7), 2543–2554.

Hsieh, W. C., A. Nenes, R. C. Flagan, J. H. Seinfeld, G. Buzorius, and H. Jonsson (2009), Parameterization of cloud droplet size distributions: Comparison with parcel models and observations, *J. Geophys. Res.*, *114*, D11205, doi:10.1029/2008JD011387.

Hudson, J. G., and S. Noble (2014), CCN and vertical velocity influences on droplet concentrations and supersaturations in clean and polluted stratus clouds, *J. Atmos. Sci.*, *71*(1), 312–331, doi:10.1175/jas-d-13-086.1.

Jacobson, M. Z., R. P. Turco, E. J. Jensen, and O. B. Toon (1994), Modeling coagulation among particles of different composition and size, *Atmos. Environ.*, *28*(7), 1327–1338, doi:10.1016/1352-2310(94)90280-1.

Khlystov, A., C. Stanier, and S. N. Pandis (2004), An algorithm for combining electrical mobility and aerodynamic size distributions data when measuring ambient aerosol special issue of aerosol science and technology on findings from the fine particulate matter supersites program, *Aerosol Sci. Technol.*, *38*(S1), 229–238.

Lance, S., C. A. Brock, D. Rogers, and J. A. Gordon (2010), Water droplet calibration of the Cloud Droplet Probe (CDP) and in-flight performance in liquid, ice and mixed-phase clouds during ARCPAC, *Atmos. Meas. Tech.*, *3*(6), 1683–1706, doi:10.5194/amt-3-1683-2010.

Leaitch, W. R., C. M. Banic, G. A. Isaac, M. D. Couture, P. S. K. Liu, I. Gultepe, S. M. Li, L. Kleinman, P. H. Daum, and J. I. MacPherson (1996), Physical and chemical observations in marine stratus during the 1993 North Atlantic Regional Experiment: Factors controlling cloud droplet number concentrations, *J. Geophys. Res.*, *101*, 29,123–29,135, doi:10.1029/96JD01228.

Leaitch, W. R., et al. (2010), Cloud albedo increase from carbonaceous aerosol, *Atmos. Chem. Phys.*, *10*(16), 7669–7684, doi:10.5194/acp-10-7669-2010.

Leck, C., and E. K. Bigg (2005), Source and evolution of the marine aerosol—A new perspective, *Geophys. Res. Lett.*, *32*, L19803, doi:10.1029/2005GL023651.

Li, X., L. Wang, D. Chen, K. Yang, B. Xue, and L. Sun (2013), Near-surface air temperature lapse rates in the mainland China during 1962–2011, *J. Geophys. Res. Atmos.*, *118*, 7505–7515, doi:10.1002/jgrd.50553.

Massling, A., M. Stock, B. Wehner, Z. J. Wu, M. Hu, E. Brueggemann, T. Gnauk, H. Herrmann, and A. Wiedensohler (2009), Size segregated water uptake of the urban submicrometer aerosol in Beijing, *Atmos. Environ.*, *43*(8), 1578–1589, doi:10.1016/j.atmosenv.2008.06.003.

McFiggans, G., et al. (2006), The effect of physical and chemical aerosol properties on warm cloud droplet activation, *Atmos. Chem. Phys.*, *6*, 2593–2649.

Ming, Y., and L. M. Russell (2004), Organic aerosol effects on fog droplet spectra, *J. Geophys. Res.*, *109*, D10206, doi:10.1029/2003JD004427.

Mochida, M., C. Nishita-Hara, H. Furutani, Y. Miyazaki, J. Jung, K. Kawamura, and M. Uematsu (2011), Hygroscopicity and cloud condensation nucleus activity of marine aerosol particles over the western North Pacific, *J. Geophys. Res.*, *116*, D06204, doi:10.1029/2010JD014759.

Modini, R. L., et al. (2015), Primary marine aerosol-cloud interactions off the coast of California, *J. Geophys. Res. Atmos.*, *120*, 4282–4303, doi:10.1002/2014JD022963.

Moffet, R. C., T. Henn, A. Laskin, and M. K. Gilles (2010), Automated chemical analysis of internally mixed aerosol particles using X-ray spectromicroscopy at the carbon K-edge, *Anal. Chem.*, *82*(19), 7906–7914, doi:10.1021/ac1012909.

Moore, R. H., and A. Nenes (2009), Scanning flow CCN analysis—A method for fast measurements of CCN spectra, *Aerosol Sci. Technol.*, *43*(12), 1192–1207, doi:10.1080/02786820903289780.

Nenes, A., and J. H. Seinfeld (2003), Parameterization of cloud droplet formation in global climate models, *J. Geophys. Res.*, *108*(D14), 4415, doi:10.1029/2002JD002911.

Nenes, A., S. N. Pandis, and C. Pilinis (1998), ISORROPIA: A new thermodynamic equilibrium model for multiphase multicomponent inorganic aerosols, *Aquat. Geochem.*, *4*(1), 123–152, doi:10.1023/a:1009604003981.

Nenes, A., S. Ghan, H. Abdul-Razzak, P. Y. Chuang, and J. H. Seinfeld (2001), Kinetic limitations on cloud droplet formation and impact on cloud albedo, *Tellus, Ser. B*, *53*(2), 133–149, doi:10.1034/j.1600-0889.2001.d01-12.x.

Nicholls, S., and J. Leighton (1986), An observational study of the structure of stratiform cloud sheets: 1. Structure, *Q. J. R. Meteorol. Soc.*, *112*(472), 431–460, doi:10.1002/qj.49711247209.

Noone, K. J., J. A. Ogren, J. Heintzenberg, R. J. Charlson, and D. S. Covert (1988), Design and calibration of a counterflow virtual impactor for sampling of atmospheric fog and cloud droplets, *Aerosol Sci. Technol.*, *8*(3), 235–244, doi:10.1080/02786828808959186.

Novakov, T., and C. E. Corrigan (1996), Cloud condensation nucleus activity of the organic component of biomass smoke particles, *Geophys. Res. Lett.*, *23*, 2141–2144, doi:10.1029/96GL01971.

Peng, Y. R., U. Lohmann, and R. Leaitch (2005), Importance of vertical velocity variations in the cloud droplet nucleation process of marine stratus clouds, *J. Geophys. Res.*, *110*, D21213, doi:10.1029/2004JD004922.

Petters, M. D., and S. M. Kreidenweis (2007), A single parameter representation of hygroscopic growth and cloud condensation nucleus activity, *Atmos. Chem. Phys.*, *7*(8), 1961–1971.

Petters, M. D., S. M. Kreidenweis, and P. J. Ziemann (2015), Prediction of cloud condensation nuclei activity for organic compounds using functional group contribution methods, *Geosci. Model Dev.*, *8*, 7445–7475, doi:10.5194/gmdd-8-7445-2015.

Prabhakar, G., B. Ervens, Z. Wang, L. C. Maudlin, M. M. Coggon, H. H. Jonsson, J. H. Seinfeld, and A. Sorooshian (2014), Sources of nitrate in stratocumulus cloud water: Airborne measurements during the 2011 E-PEACE and 2013 NiCE studies, *Atmos. Environ.*, *97*, 166–173, doi:10.1016/j.atmosenv.2014.08.019.

Quinn, P. K., T. S. Bates, K. S. Schulz, D. J. Coffman, A. A. Frossard, L. M. Russell, W. C. Keene, and D. J. Kieber (2014), Contribution of sea surface carbon pool to organic matter enrichment in sea spray aerosol, *Nat. Geosci.*, *7*(3), 228–232, doi:10.1038/ngeo2092.

Raatikainen, T., et al. (2013), Worldwide data sets constrain the water vapor uptake coefficient in cloud formation, *Proc. Natl. Acad. Sci. U.S.A.*, *110*(10), 3760–3764, doi:10.1073/pnas.1219591110.

Raymond, T. M., and S. N. Pandis (2002), Cloud activation of single-component organic aerosol particles, *J. Geophys. Res.*, *107*(D24), 4787, doi:10.1029/2002JD002159.

Reutter, P., H. Su, J. Trentmann, M. Simmel, D. Rose, S. S. Gunthe, H. Wernli, M. O. Andreae, and U. Poeschl (2009), Aerosol- and updraft-limited regimes of cloud droplet formation: Influence of particle number, size and hygroscopicity on the activation of cloud condensation nuclei (CCN), *Atmos. Chem. Phys.*, *9*(18), 7067–7080.

Rissman, T. A., A. Nenes, and J. H. Seinfeld (2004), Chemical amplification (or dampening) of the Twomey effect: Conditions derived from droplet activation theory, *J. Atmos. Sci.*, *61*(8), 919–930, doi:10.1175/1520-0469(2004)061<0919:caodot>2.0.co;2.

Russell, L. M., and J. H. Seinfeld (1998), Size- and composition-resolved externally mixed aerosol model, *Aerosol Sci. Technol.*, *28*(5), 403–416, doi:10.1080/02786829808965534.

Russell, L. M., et al. (1999), Aerosol dynamics in ship tracks, *J. Geophys. Res.*, *104*, 31,077–31,095, doi:10.1029/1999JD900985.

Russell, L. M., et al. (2013), Eastern Pacific emitted aerosol cloud experiment, *Bull. Am. Meteorol. Soc.*, *94*(5), 709–729, doi:10.1175/bams-d-12-00015.1.

Schroder, J. C., S. J. Hanna, R. L. Modini, A. L. Corrigan, A. M. Macdonald, K. J. Noone, L. M. Russell, W. R. Leaitch, and A. K. Bertram (2014), Size-resolved observations of refractory black carbon particles in cloud droplets at a marine boundary layer site, *Atmos. Chem. Phys. Discuss.*, *14*(8), 11,447–11,491, doi:10.5194/acpd-14-11447-2014.

Shingler, T., et al. (2012), Characterisation and airborne deployment of a new counterflow virtual impactor inlet, *Atmos. Meas. Tech.*, *5*(6), 1259–1269, doi:10.5194/amt-5-1259-2012.

Shulman, M. L., M. C. Jacobson, R. J. Carlson, R. E. Synovec, and T. E. Young (1996), Dissolution behavior and surface tension effects of organic compounds in nucleating cloud droplets, *Geophys. Res. Lett.*, *23*, 277–280, doi:10.1029/95GL03810.

Snider, J. R., S. Guibert, J. L. Brenguier, and J. P. Putaud (2003), Aerosol activation in marine stratocumulus clouds: 2. Kohler and parcel theory closure studies, *J. Geophys. Res.*, *108*(D15), 8629, doi:10.1029/2002JD002692.

Sorooshian, A., Z. Wang, M. M. Coggon, H. H. Jonsson, and B. Ervens (2013), Observations of sharp oxalate reductions in stratocumulus clouds at variable altitudes: Organic acid and metal measurements during the 2011 E-PEACE Campaign, *Environ. Sci. Technol.*, *47*(14), 7747–7756, doi:10.1021/es4012383.

Sorooshian, A., E. Crosbie, L. C. Maudlin, J.-S. Youn, Z. Wang, T. Shingler, A. M. Ortega, S. Hersey, and R. K. Woods (2015), Surface and airborne measurements of organosulfur and methanesulfonate over the western United States and coastal areas, *J. Geophys. Res. Atmos.*, *120*, 8535–8548, doi:10.1002/2015JD023822.

Tiitta, P., et al. (2010), Roadside aerosol study using hygroscopic, organic and volatility TDMAs: Characterization and mixing state, *Atmos. Environ.*, *44*(7), 976–986, doi:10.1016/j.atmosenv.2009.06.021.

Twohy, C. H., et al. (2013), Impacts of aerosol particles on the microphysical and radiative properties of stratocumulus clouds over the southeast Pacific Ocean, *Atmos. Chem. Phys.*, *13*(5), 2541–2562, doi:10.5194/acp-13-2541-2013.

Twomey, S. (1977), *Atmospheric Aerosols (Developments in Atmospheric Science)*, 316 pp., Elsevier Sci., Amsterdam.

Tzivion, S., G. Feingold, and Z. Levin (1987), An efficient numerical solution to the stochastic collection equation, *J. Atmos. Sci.*, *44*(21), 3139–3149, doi:10.1175/1520-0469(1987)044<3139:aenstt>2.0.co;2.

VanReken, T. M., T. A. Rissman, G. C. Roberts, V. Varutbangkul, H. H. Jonsson, R. C. Flagan, and J. H. Seinfeld (2003), Toward aerosol/cloud condensation nuclei (CCN) closure during CRYSTAL-FACE, *J. Geophys. Res.*, *108*(D20), 4633, doi:10.1029/2003JD003582.

Wang, J., M. J. Cubison, A. C. Aiken, J. L. Jimenez, and D. R. Collins (2010), The importance of aerosol mixing state and size-resolved composition on CCN concentration and the variation of the importance with atmospheric aging of aerosols, *Atmos. Chem. Phys.*, *10*(15), 7267–7283, doi:10.5194/acp-10-7267-2010.

West, R. E. L., P. Stier, A. Jones, C. E. Johnson, G. W. Mann, N. Bellouin, D. G. Partridge, and Z. Kipling (2014), The importance of vertical velocity variability for estimates of the indirect aerosol effects, *Atmos. Chem. Phys.*, *14*(12), 6369–6393, doi:10.5194/acp-14-6369-2014.

Wonaschuetz, A., et al. (2013), Hygroscopic properties of smoke-generated organic aerosol particles emitted in the marine atmosphere, *Atmos. Chem. Phys.*, *13*(19), 9819–9835, doi:10.5194/acp-13-9819-2013.

Youn, J. S., E. Crosbie, L. C. Maudlin, Z. Wang, and A. Sorooshian (2015), *Dimethylamine* as a major alkyl amine species in particles and cloud water: Observations in semi-arid and coastal regions, *Atmos. Environ.*, *122*, 250–258, doi:10.1016/j.atmosenv.2015.09.061.